



## A new warm-cloud collection and breakup parameterization scheme for weather and climate models

Han-Gyul Jin <sup>a</sup>, Jong-Jin Baik <sup>a,\*</sup>, Hyunho Lee <sup>b</sup>, Tanvir Ahmed <sup>a,c</sup>

<sup>a</sup> School of Earth and Environmental Sciences, Seoul National University, Seoul 08826, South Korea

<sup>b</sup> Department of Atmospheric Science, Kongju National University, Gongju 32588, South Korea

<sup>c</sup> Department of Physics, Shahjalal University of Science and Technology, Sylhet 3114, Bangladesh



### ARTICLE INFO

#### Keywords:

Warm-cloud microphysics  
Collection parameterization  
Breakup parameterization  
Bulk microphysics scheme  
Shallow convective cloud

### ABSTRACT

Microphysical process rates in bulk microphysics schemes have been parameterized in simple forms which may inadequately represent their complicated dependencies on hydrometeor quantities. In this study, we develop a bulk warm rain microphysics scheme that includes physically based parameterizations of collection and breakup. The parameterizations are derived from the stochastic collection and breakup equations by approximating the collection and breakup kernels in elaborate forms and analytically evaluating the integrals in those equations. Although the new scheme performs relatively complicated calculations, it is computationally not too expensive to be used in weather and climate models. We first evaluate the raindrop self-collection and collisional breakup (RSCB) parameterizations developed in this study using a box model. Under the intrinsic limitation of bulk schemes, they generally yield the equilibrium raindrop size distributions closest to those from a bin-based solver. We then evaluate the new scheme through the simulations of shallow cumuli field and a single warm convective cloud. In the simulation of shallow cumuli field, the new scheme quite well reproduces the observed cloud properties. Compared to two other bulk schemes, the new scheme yields somewhat different rainwater mass and raindrop number concentration, which is largely attributable to the differences in autoconversion parameterizations. In the simulation of a single warm convective cloud where RSCB plays a major role, the rate of raindrop number depletion by RSCB and the time of precipitation onset predicted by the new scheme are close to those predicted by a bin scheme used as the reference.

### 1. Introduction

Better representing the microphysics of warm (liquid-only) clouds in numerical models has been, and still is, the goal of numerous studies due to its importance to hydrological cycle and radiation (e.g., Khairoutdinov and Kogan, 2000; Noh et al., 2018; Kogan and Ovchinnikov, 2020). The microphysical processes in warm clouds include droplet activation, vapor diffusion, collection, breakup, and sedimentation processes, each of which is parameterized in cloud microphysics schemes. Some challenges in the representation of warm-cloud microphysics stem from the fact that these microphysical process rates are very difficult to directly observe (Morrison et al., 2020), which leads to large uncertainties in the parameterizations of these processes in cloud microphysics schemes.

Bulk microphysics schemes are one category of cloud microphysics schemes that have been exclusively used in operational weather and climate models. Because early bulk schemes prognosed only one quantity for each hydrometeor category (i.e., one-moment bulk schemes), the mass mixing ratio, the microphysical process rates used to be expressed in simple forms, such as power-law relations for collection processes (e.g., Kessler, 1969; Tripoli and Cotton, 1980). Over a past few decades, two-moment and even three-moment bulk schemes that prognose additional quantities such as the number concentration and radar reflectivity factor for each hydrometeor category were developed (e.g., Cohard and Pinty, 2000; Milbrandt and Yau, 2005; Naumann and Seifert, 2016), but the parameterizations for the microphysical process rates often remained in relatively simple forms. The accretion rate, for example, the rate of bulk mass change in raindrops as a result of

\* Corresponding author.

E-mail address: [jjbaik@snu.ac.kr](mailto:jjbaik@snu.ac.kr) (J.-J. Baik).

collecting cloud droplets, is still represented as a function of cloud water and rainwater mass mixing ratios only in most of the multi-moment bulk schemes (e.g., Seifert and Beheng, 2006, SB06 hereafter; Kogan, 2013, K13 hereafter) although they should depend not only on the mass mixing ratios but also on the number concentrations of cloud droplets and raindrops (Ahmed et al., 2020, A20 hereafter). To make a good use of the increased number of prognostic hydrometeor quantities which gives better representations of the particle size distributions of hydrometeors, more sophisticated and physically based parameterizations of the microphysical process rates are needed.

With regard to the collection growth of hydrometeors, Verlinde et al. (1990) derived a sophisticated parameterization that includes the dependence of the growth rate on many parameters in particle size distributions and terminal velocity relations by analytically evaluating the integrals in the stochastic collection equation (SCE). This parameterization was, however, computationally too expensive to be included in operational bulk schemes (Gaudet and Schmidt, 2005). Recently, a parameterization of the autoconversion process, which is the collision-coalescence between cloud droplets producing a raindrop, was proposed by Lee and Baik (2017, LB17 hereafter). This parameterization was also derived from the SCE and had a more complicated form than previously used autoconversion parameterizations, but it was computationally not too expensive to be used in weather and climate models. Analytic approximation of collection efficiency between two colliding cloud droplets that varies with their individual sizes was a key point of LB17 parameterization. A20 used a similar approach to that of LB17 to derive an accretion parameterization from the analytic approximation of the SCE. This accretion parameterization managed to predict a wide variety of accretion rates for given mass mixing ratios of cloud water and rainwater by considering their dependence on the number concentrations of cloud droplets and raindrops. Jin and Baik (2020) who applied a similar approach to develop a parameterization of accretion of cloud water by snow showed that previous parameterizations based on relatively simple forms of collection equation cannot appropriately reproduce the change in the number concentration of collected droplets predicted by a bin-based direct SCE solver while the developed parameterization can.

The collisional breakup process of raindrops, another important warm-cloud microphysical process, has been usually expressed in an implicit way in bulk schemes. Most bulk schemes parameterize the raindrop collisional breakup together with the raindrop self-collection by simply adjusting the bulk self-collection efficiency in the raindrop self-collection parameterization according to the mean raindrop diameter (Morrison et al., 2005; Milbrandt and Yau, 2005; Thompson et al., 2008), following Verlinde and Cotton (1993, VC93 hereafter) and Cohard and Pinty (2000). The complexity of the collisional breakup equation, where the number of fragment drops as a result of the collision as well as the coalescence efficiency must be considered (Hu and Srivastava, 1995), has made it difficult to obtain a parameterization for use in bulk schemes using an analytic approximation approach. Feingold et al. (1988) obtained an analytic solution of an approximated stochastic breakup equation, but this equation was considerably simplified by assuming a constant breakup kernel and choosing a simple function for the size distribution of fragment drops. Recently, Paukert et al. (2019) developed an explicit parameterization of the raindrop self-collection and collisional breakup (RSCB) processes using a lookup table approach. A lookup table approach based on the bin model outputs (e.g., Khain et al., 2004) can be a good alternative to the analytic approximation approach when it is not available, because this approach can also consider the parameterization's dependencies on several bulk quantities of raindrops. Apart from this approach, however, an analytic

approximation approach is needed because a parameterization derived using this approach gives a physical insight to the corresponding microphysical process and is more flexible to changes in the parameters or assumptions used (Seifert et al., 2014).

This study aims to establish a bulk microphysics scheme for warm clouds that consists of more sophisticated and physically based collection and breakup parameterizations. This scheme includes the autoconversion (LB17) and accretion (A20) parameterizations that were developed using the analytic approximation approach and a new RSCB parameterization that is developed in this study using a similar approach to those in LB17 and A20. Michibata and Takemura (2015) found that a different choice of autoconversion parameterization results in a substantially different prediction in the general circulation model simulation, implying high uncertainties from the parameterizations of microphysical process rates. The parameterizations tested there were in relatively simple forms, either derived from simplified collection equations or fitted to bin model outputs. For example, the parameterizations of Khairoutdinov and Kogan (2000) are in the forms of simple power-law equations of which the coefficients were obtained by fitting to the data of bin model simulations of marine boundary layer stratocumulus clouds. The new scheme with more sophisticated collection and breakup parameterizations is expected to have less uncertainties from the microphysical process rates, or at least narrow the potential source of the uncertainties.

The remainder of this paper is organized as follows. In the next section, detailed descriptions of the new warm-cloud microphysics scheme are given, along with the derivation of the new RSCB parameterization. The new RSCB parameterization is evaluated through box model simulations in Section 3. The evaluation of the new scheme that includes the LB17 autoconversion, the A20 accretion, and the new RSCB parameterizations is done through two sets of warm cloud simulations. The first one is the simulations of a shallow cumuli field in which the autoconversion and accretion processes play major roles while RSCB plays a minor role. Section 4 is dedicated to the model setup and results of the shallow cumuli field simulation with the new scheme and the same simulations but with previous collection and breakup parameterizations conducted for comparison. The second one is the simulations of a single warm convective cloud with a higher cloud top and larger liquid water path in which RSCB plays a major role. The model setup and results of the single warm convective cloud simulations with the new and previous schemes as well as a bin scheme are presented in Section 5. Summary and conclusions are given in Section 6.

## 2. Scheme description

In this section, descriptions of a new bulk cloud microphysics scheme with warm-cloud collection and breakup parameterizations are provided. The particle size distributions and terminal velocity relations assumed in this scheme are identical to those in LB17 and A20. The cloud droplet and raindrop size distributions are expressed by three-parameter gamma size distributions as follows:

$$f_c(R) = N_{0,c} R^{\mu_c} \exp(-\lambda_c R), \quad (1)$$

$$f_r(R) = N_{0,r} R^{\mu_r} \exp(-\lambda_r R), \quad (2)$$

where  $N_0$ ,  $\mu$ , and  $\lambda$  are the intercept, shape, and slope parameters of gamma size distributions, respectively,  $R$  is the particle radius, and the subscripts "c" and "r" refer to cloud droplet (or cloud water) and raindrop (or rainwater), respectively. For convenience, the list of symbols is provided in Table A1 in the Appendix. The shape parameters ( $\mu$ ) can either be fixed to any constant or diagnosed. For the simulations in this

study,  $\mu_c$  is diagnosed by the empirical relationship used in Thompson et al. (2008), that is,  $\mu_c = \min[15, \text{nint}(10^9/N_c + 2)]$  where  $N$  is the number concentration in unit of  $\text{m}^{-3}$  and  $\text{nint}(x)$  is the nearest integer of  $x$ , and  $\mu_r$  is fixed to 1. The terminal velocity relations of cloud droplets and raindrops are, respectively, given as

$$v_{t,c} = v_{0,c} R^2, \quad (3)$$

$$v_{t,r} = v_{0,r} [1 - \exp(-\gamma_r R)], \quad (4)$$

where the values of  $v_{0,c}$ ,  $v_{0,r}$ , and  $\gamma_r$  are  $1.0973 \times 10^8 \text{ m}^{-1} \text{ s}^{-1}$ ,  $9.770 \text{ m s}^{-1}$ , and  $1.097 \times 10^3 \text{ m}^{-1}$ , respectively, when  $v_{t,c}$ ,  $v_{t,r}$ , and  $R$  are in mks units. These values are obtained by nonlinear curve fitting to the data from the terminal velocity relation of Beard (1976). The use of an asymptotic function for the raindrop terminal velocity relation can prevent substantial deviations from realistic values for large raindrops, which appear in the commonly used power-law relations. The evaluation of the fitted terminal velocity relations is given in A20.

### 2.1. Autoconversion and accretion parameterizations

For the parameterization of the autoconversion process, the LB17 parameterization which was derived by analytically evaluating the integrals in the SCE is used. In this parameterization, the collision efficiency between two cloud droplets is expressed as a function of their individual sizes. The collision efficiency relation is obtained by fitting to the reference collision efficiency data of Pinsky et al. (2001) estimated by a particle trajectory model. The coalescence efficiency between cloud droplets is assumed to be unity, which makes the collection efficiency identical to the collision efficiency. There is some uncertainty in this assumption due to the lack of experimental evidence for coalescence efficiency, but the parameterization can be improved in the future when a more rigorous assumption may be made. Note that the LB17 autoconversion parameterization includes the parameterization of the self-collection process of cloud droplets. A detailed derivation and the process rate equations are provided in LB17. In this study, a threshold value of mean volume cloud droplet radius ( $10 \mu\text{m}$ ) below which the autoconversion rate is assumed to be zero is applied to the LB17 autoconversion parameterization following the method of Tripoli and Cotton (1980). This prevents unexpected overestimations of autoconversion rate when the mean cloud droplet size is very small.

For the accretion parameterization, the A20 parameterization is used. This parameterization uses the similar approach to that of LB17, while not only the collision efficiency data of Pinsky et al. (2001) but also those of Beard and Grover (1974) are adopted as the reference collision efficiency, in order to cover the wide size range of raindrops. Also in the A20 parameterization, the coalescence efficiency is assumed to be unity, supported by the direct numerical simulations (DNS) by Straub et al. (2010) for drop collisions based on the “volume of fluid” method, which showed the coalescence efficiency close to 1 for small Weber numbers in the accretion regime. A detailed derivation and the process rate equations are provided in A20.

### 2.2. Raindrop self-collection and collisional breakup (RSCB) parameterization

The governing equation for the evolution of raindrop number concentration through the self-collection and breakup processes can be expressed by the SCE and stochastic breakup equation (SBE) as (Hu and Srivastava, 1995):

$$\begin{aligned} \frac{\partial f_r(m, t)}{\partial t} = & \frac{1}{2} \int_0^m f_r(m', t) f_r(m - m', t) C(m', m - m') dm' \\ & - f_r(m, t) \int_0^\infty f_r(m', t) C(m, m') dm' \\ & + \frac{1}{2} \int_0^\infty \int_0^\infty f_r(m', t) f_r(m'', t) B(m', m'') P(m; m', m'') dm' dm'' \\ & - f_r(m, t) \int_0^\infty f_r(m', t) B(m, m') dm', \end{aligned} \quad (5)$$

where  $C(m, m')$  and  $B(m, m')$  are the coalescence kernel and the breakup kernel between two raindrops with masses  $m$  and  $m'$ , respectively, and  $P(m; m', m'')$  is the average number of fragment drops with mass  $m$  produced as a result of the collision of two raindrops with masses  $m'$  and  $m''$ , respectively. Here, the raindrop size distribution is expressed as a function of raindrop mass and time:  $f_r(m, t)$ . The first two terms in the right hand side of Eq. (5) are from the SCE, and the last two terms are from the SBE. Integrating Eq. (5) over the raindrop mass gives the rate of change in the total number concentration of raindrops through RSCB. By changing the mass variables to radius variables, it is written as

$$\begin{aligned} \left. \frac{\partial N_r}{\partial t} \right|_{\text{RSCB}} = & - \int_0^\infty \int_0^R f_r(r, t) f_r(R, t) C(r, R) dr dR \\ & + \frac{1}{2} \int_0^\infty \int_0^\infty f_r(r, t) f_r(R, t) B(r, R) [\bar{N}_f(r, R) - 2] dr dR, \end{aligned} \quad (6)$$

where  $\bar{N}_f$  is the (average) number of fragment drops with any size as a result of the collision between two raindrops with radii  $r$  and  $R$ . The derivation of Eq. (6) is described in Appendix A.

The coalescence kernel and breakup kernel are determined by the collision cross-section area, terminal velocity difference, and collision and coalescence efficiency of two colliding raindrops as follows:

$$C(r, R) = \pi(r + R)^2 |v_{t,r}(r) - v_{t,r}(R)| \eta_{\text{coll}} \eta_{\text{coal}}, \quad (7)$$

$$B(r, R) = \pi(r + R)^2 |v_{t,r}(r) - v_{t,r}(R)| \eta_{\text{coll}} (1 - \eta_{\text{coal}}), \quad (8)$$

where  $\eta_{\text{coll}}$  and  $\eta_{\text{coal}}$  are the collision and coalescence efficiency, respectively. For the collision between raindrops, the collision efficiency is assumed to be 1, considering that raindrops with relatively large inertia are not likely to be affected much by the flow fields around other raindrops. On the other hand, the coalescence efficiency can be much smaller than 1 when the two raindrops collide into each other strongly enough so that the temporarily-coalesced system cannot be maintained and eventually splits into fragment drops (Schlottke et al., 2010).

Therefore, to evaluate the integrals in Eq. (6) analytically, each of the coalescence efficiency and the fragment drop number must be expressed as a function of the individual sizes of two colliding raindrops. For this, the parameterizations of Seifert et al. (2005, S05 hereafter), which are combinations of the empirical parameterizations of Low and List (1982) and Beard and Ochs III (1995), are used (Eqs. (5) and (6) in S05). For example, the coalescence efficiency parameterization of S05 is threefold according to the diameter of the smaller raindrop of two colliding raindrops: the Beard and Ochs III (1995) parameterization when the diameter is smaller than  $300 \mu\text{m}$ , the Low and List (1982) parameterization when the diameter is larger than  $600 \mu\text{m}$ , and the combination of

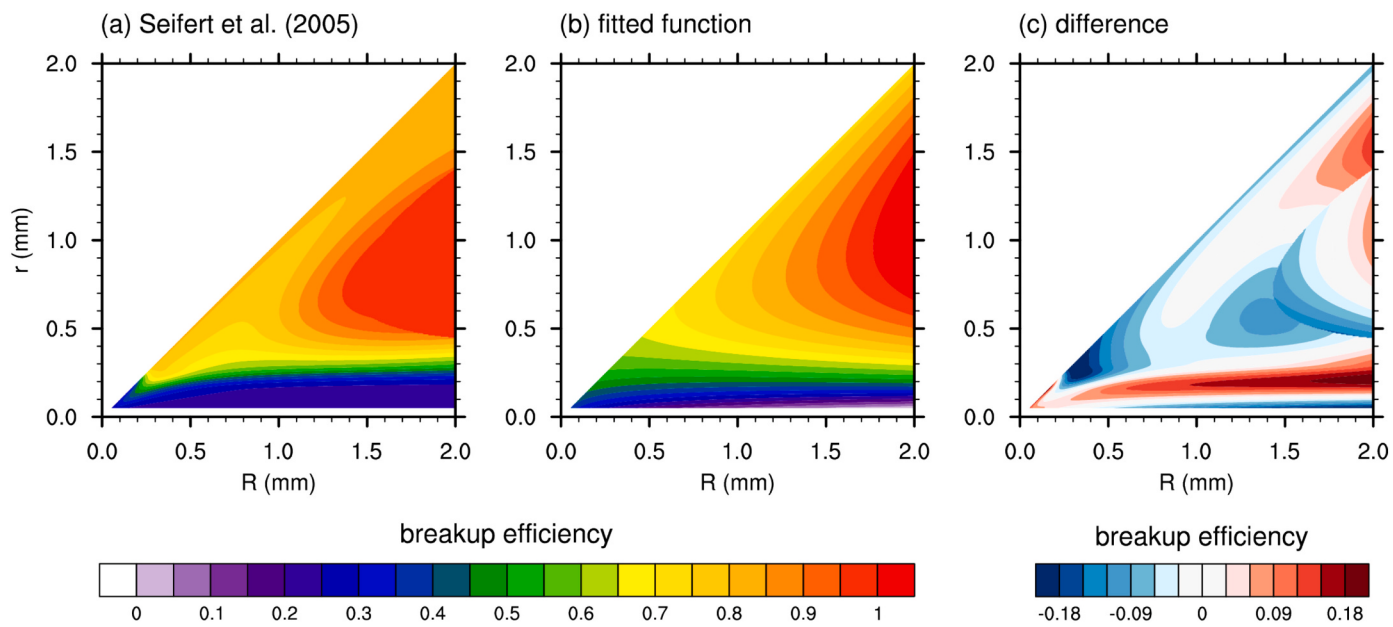


**Fig. 1.** Breakup efficiency between raindrops with radii of  $R$  and  $r$  from (a) Seifert et al. (2005) and (b) the fitted function. (c) The fitted breakup efficiency minus the breakup efficiency from Seifert et al. (2005).

the two parameterizations when the diameter is intermediate. In these parameterizations, the Weber number and the collision kinetic energy are employed to represent the coalescence efficiency and the number of fragment drops. Because the S05 parameterizations are too complex to be directly implemented into Eq. (6), new functions are introduced in this study and fitted to the S05 parameterizations. Then, the breakup efficiency  $\eta_{\text{break}}$ , which is unity minus the coalescence efficiency, is expressed as

$$\eta_{\text{break}} = 1 - \eta_{\text{coal}} = a_0 + a_1 r (a_2 R - r) - a_3 R^{a_4} \exp(-a_5 R), \quad (9)$$

where the coefficients  $a_0$ ,  $a_1$ ,  $a_2$ ,  $a_3$ ,  $a_4$ , and  $a_5$  are  $7.50 \times 10^{-1}$ ,  $3.54 \times 10^5 \text{ m}^{-2}$ ,  $9.85 \times 10^{-1}$ ,  $3.61 \text{ m}^{-a_4}$ ,  $2.13 \times 10^{-1}$ , and  $4.30 \times 10^3 \text{ m}^{-1}$ ,

respectively, when  $R$  and  $r$  are in meters. Fig. 1 shows the reference breakup efficiency from S05, the fitted breakup efficiency, and the difference between them. Overall, the fitted function for the breakup efficiency agrees well with the reference and has the coefficient of determination of 0.90.

The number of fragment drops  $\bar{N}_f$  is expressed as

$$\bar{N}_f = 2 + b_0 \left(1 - \frac{r}{R}\right) R^3 r^3 \exp(-b_1 R) \exp(-b_2 r) + b_3 R^{12} r^6 \exp(-b_4 R) \exp(-b_5 r), \quad (10)$$

where the coefficients  $b_0$ ,  $b_1$ ,  $b_2$ ,  $b_3$ ,  $b_4$ , and  $b_5$  are  $5.00 \times 10^{19} \text{ m}^{-6}$ ,  $5.26 \times 10^1 \text{ m}^{-1}$ ,  $2.89 \times 10^3 \text{ m}^{-1}$ ,  $1.50 \times 10^{65} \text{ m}^{-18}$ ,  $1.16 \times 10^4 \text{ m}^{-1}$ , and  $2.09 \times 10^4 \text{ m}^{-1}$ , respectively, when  $R$  and  $r$  are in meters. The fitted

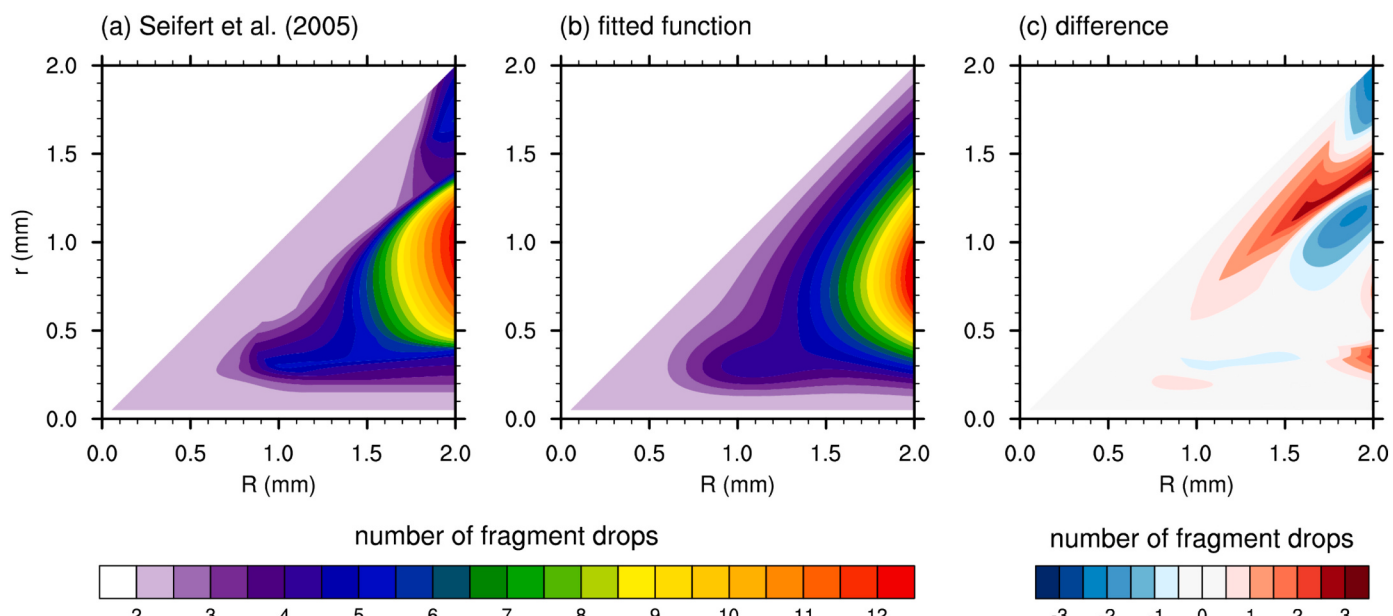


**Fig. 2.** Number of fragment drops produced as a result of collision between raindrops with radii of  $R$  and  $r$  from (a) Seifert et al. (2005) and (b) the fitted function. (c) The fitted fragment drop number minus the fragment drop number from Seifert et al. (2005).

function for the number of fragment drops well reproduces the reference from S05, with the coefficient of determination being 0.90 (Fig. 2).

Using the parameterized  $\eta_{\text{break}}$  and  $\bar{N}_f$ , the integrals in Eq. (6) can be solved, which gives the RSCB rate expressed as

$$\frac{\partial N_r}{\partial t} \Big|_{\text{RSCB}} = \pi \left( \frac{\rho_0}{\rho} \right)^{1/2} N_{0,r}^2 v_{0,r} [N_{\text{break}} - (N_{\text{self},1} + N_{\text{self},2} + N_{\text{self},3})], \quad (11)$$

where

$$N_{\text{break}} = \sum_{i=1}^{12} \sum_{j=0}^2 c_{0,i} A_j \left\{ \Gamma_1(\lambda_r + c_{4,i} + \gamma_r, \mu_r + c_{2,i} + 1 + j) \times [\Gamma_1(\lambda_r + c_{3,i}, \mu_r + c_{1,i} + 3 - j) - \sum_{k=0}^{\mu_r + c_{2,i} + j} \frac{(\lambda_r + c_{4,i} + \gamma_r)^k}{\Gamma(k+1)} \Gamma_1(2\lambda_r + c_{3,i} + c_{4,i} + \gamma_r, \mu_r + c_{1,i} + 3 - j + k)] - \Gamma_1(\lambda_r + c_{4,i}, \mu_r + c_{2,i} + 1 + j) \times [\Gamma_1(\lambda_r + c_{3,i} + \gamma_r, \mu_r + c_{1,i} + 3 - j) - \sum_{k=0}^{\mu_r + c_{2,i} + j} \frac{(\lambda_r + c_{4,i})^k}{\Gamma(k+1)} \Gamma_1(2\lambda_r + c_{3,i} + c_{4,i} + \gamma_r, \mu_r + c_{1,i} + 3 - j + k)] \right\}, \quad (12)$$

$$N_{\text{self},1} = (1 - a_0) \sum_{j=0}^2 A_j \left\{ \Gamma_1(\lambda_r + \gamma_r, \mu_r + 1 + j) \times [\Gamma_1(\lambda_r, \mu_r + 3 - j) - \sum_{k=0}^{\mu_r + j} \frac{(\lambda_r + \gamma_r)^k}{\Gamma(k+1)} \Gamma_1(2\lambda_r + \gamma_r, \mu_r + 3 - j + k)] - \Gamma_1(\lambda_r, \mu_r + 1 + j) \times [\Gamma_1(\lambda_r + \gamma_r, \mu_r + 3 - j) - \sum_{k=0}^{\mu_r + j} \frac{\lambda_r^k}{\Gamma(k+1)} \Gamma_1(2\lambda_r + \gamma_r, \mu_r + 3 - j + k)] \right\}, \quad (13)$$

$$N_{\text{self},2} = a_3 \sum_{j=0}^2 A_j \left\{ \Gamma_1(\lambda_r + a_5 + \gamma_r, \mu_r + 1 + j) \times [\Gamma_1(\lambda_r, \mu_r + a_4 + 3 - j) - \sum_{k=0}^{\mu_r + j} \frac{(\lambda_r + a_5 + \gamma_r)^k}{\Gamma(k+1)} \Gamma_1(2\lambda_r + a_5 + \gamma_r, \mu_r + a_4 + 3 - j + k)] - \Gamma_1(\lambda_r + a_5, \mu_r + 1 + j) \times [\Gamma_1(\lambda_r + \gamma_r, \mu_r + a_4 + 3 - j) - \sum_{k=0}^{\mu_r + j} \frac{(\lambda_r + a_5)^k}{\Gamma(k+1)} \Gamma_1(2\lambda_r + \gamma_r, \mu_r + a_4 + 3 - j + k)] \right\}, \quad (14)$$

**Table 1**  
Coefficients used in Eq. (12).

i	Coefficients				
	$c_{0,i}$	$c_{1,i}$	$c_{2,i}$	$c_{3,i}$	$c_{4,i}$
1	$a_0 b_0$	3	3	$b_1$	$b_2$
2	$a_1 a_2 b_0$	4	4	$b_1$	$b_2$
3	$-a_1 b_0$	3	5	$b_1$	$b_2$
4	$-a_3 b_0$	$a_4 + 3$	3	$b_1$	$a_5 + b_2$
5	$a_0 b_0$	2	4	$b_1$	$b_2$
6	$a_1 a_2 b_0$	3	5	$b_1$	$b_2$
7	$-a_1 b_0$	2	6	$b_1$	$b_2$
8	$-a_3 b_0$	$a_4 + 2$	4	$b_1$	$a_5 + b_2$
9	$a_0 b_3$	12	6	$b_4$	$b_5$
10	$a_1 a_2 b_3$	13	7	$b_4$	$b_5$
11	$-a_1 b_3$	12	8	$b_4$	$b_5$
12	$-a_3 b_3$	$a_4 + 12$	6	$b_4$	$a_5 + b_5$

$$N_{\text{self},3} = a_1 \sum_{j=0}^3 B_j \left\{ \Gamma_1(\lambda_r + \gamma_r, \mu_r + 2 + j) \times [\Gamma_1(\lambda_r, \mu_r + 4 - j) - \sum_{k=0}^{\mu_r + j} \frac{(\lambda_r + \gamma_r)^k}{\Gamma(k+1)} \Gamma_1(2\lambda_r + \gamma_r, \mu_r + 4 - j + k)] - \Gamma_1(\lambda_r, \mu_r + 2 + j) \times [\Gamma_1(\lambda_r + \gamma_r, \mu_r + 4 - j) - \sum_{k=0}^{\mu_r + j} \frac{\lambda_r^k}{\Gamma(k+1)} \Gamma_1(2\lambda_r + \gamma_r, \mu_r + 4 - j + k)] \right\}. \quad (15)$$

Here,  $A_j$  is given as  $(A_0, A_1, A_2) = (1, 2, 1)$ ,  $B_j$  is given as  $(B_0, B_1, B_2, B_3) = (-a_2, 1 - 2a_2, 2 - a_2, 1)$ , and  $c_{0,i}$ ,  $c_{1,i}$ ,  $c_{2,i}$ ,  $c_{3,i}$ , and  $c_{4,i}$  are given in Table 1. The function  $\Gamma_1(\lambda, s)$  is defined as

$$\Gamma_1(\lambda, s) = \frac{\Gamma(s)}{\lambda^s}, \quad (16)$$

where  $\Gamma$  is the gamma function and  $s > 0$ . In Eq. (11), the air density factor  $(\rho_0/\rho)^{1/2}$  is included to describe the terminal velocity increase related to the air density decrease, where  $\rho_0$  is the reference air density and  $\rho$  is the air density. The rainwater mass is not affected by RSCB. The evaluation of the new RSCB parameterization is given in Section 3.

### 2.3. Other microphysical processes

The droplet activation, condensation, and evaporation parameterizations in this scheme follow those of Morrison and Grabowski (2007, 2008), as implemented in the Predicted Particle Properties (P3) micro-physics scheme (Morrison and Milbrandt, 2015). The spectrum of cloud condensation nuclei (CCN) and their chemical properties are prescribed and unchanged during the model integration. The amount of activated CCN is determined explicitly by the supersaturation following the Köhler theory (Köhler, 1936), assuming that the local  $N_c$  is the concentration of previously activated CCN. The condensation and evaporation rates are computed from the semi-analytic parameterization that employs the supersaturation relaxation time scales (Morrison and Grabowski, 2008; Morrison and Milbrandt, 2015). The mass mixing ratios and number concentrations of liquid hydrometeors sediment at mass-weighted and number-weighted mean terminal velocities, respectively.

### 3. Evaluation of the new RSCB parameterization

The newly developed RSCB parameterization is evaluated through box model simulations where RSCB is the only microphysical process allowed and is compared with two previous RSCB parameterizations. One of the previous RSCB parameterizations considered is a combination of the self-collection parameterization of Beheng (1994, B94 hereafter) and the breakup parameterization of VC93, which has been adopted by many bulk microphysics schemes (e.g., Morrison et al., 2005; Thompson et al., 2008). The B94/VC93 RSCB parameterization employs the bulk self-collection efficiency. This bulk self-collection efficiency is 1 when the mean raindrop diameter is smaller than a threshold diameter, and it becomes smaller and can even be negative as the mean raindrop diameter exceeds the threshold diameter. The bulk self-collection efficiency smaller than 1 implies the activation of the breakup process. The threshold mean volume diameter is set to 0.6 mm. The other previous RSCB parameterization is one derived by SB06 and later corrected by Kuba et al. (2020). The SB06 RSCB parameterization uses a breakup function that plays a similar role as the negative of the bulk self-collection efficiency, but the breakup function is obtained based on bin model outputs. Because the new and SB06 RSCB parameterizations can be used not only for the exponential size distribution of raindrops but also for gamma size distributions of raindrops with various shape parameters,  $\mu_r = 0$  and  $\mu_r = 1$  which are widely used in bulk micro-physics schemes are tested for these two RSCB parameterizations. The

new RSCB parameterization is also compared with a bin-based numerical solution of SCE and SBE by Seifert et al. (2005). For this numerical solution, the drop mass coordinate is discretized, where the mass doubles every third bin, and the methods of Bott (1998) and Bleck (1970) are used for solving the SCE and SBE, respectively.

The initial rainwater mass content is fixed to  $2 \text{ g m}^{-3}$ , and the initial mass-weighted mean raindrop diameters ranging from 0.5 to 4 mm are tested. The time step is 1 s. For each simulation, the model is integrated until the mass-weighted mean raindrop diameter  $D_{m,r}$  becomes almost stationary ( $|\Delta D_{m,r}| < 10^{-4} \text{ mm}$  during a single time step).  $D_{m,r}$  at the stationary state is defined as the equilibrium diameter.

In bulk microphysics schemes, only a few parameters in the prescribed raindrop size distributions can evolve due to RSCB. Because of this inherent limitation of bulk microphysics schemes, the outcome of RSCB may not be perfectly represented by bulk parameterizations. Fig. 3 shows the raindrop size distributions at the stationary state, the equilibrium raindrop size distributions (ERSDs), calculated using the RSCB parameterizations and the bin-based solver of Seifert et al. (2005). The ERSD is known to have two or three modes (Feingold et al., 1988; McFarquhar, 2004; Prat and Barros, 2007), which is also shown by the bin-based solver. For each  $\mu_r$ , all of the RSCB parameterizations show similar ERSDs, while the new RSCB parameterization tends to show slightly higher number concentrations of small raindrops and slightly lower number concentrations of large raindrops compared to the other RSCB parameterizations. Compared to the ERSD of the bin-based solver, when an exponential size distribution of raindrops is assumed ( $\mu_r = 0$ ), overestimations of the number concentration of raindrops with  $D$  (diameter)  $> \sim 2.8 \text{ mm}$  and with  $D < \sim 0.2 \text{ mm}$  by the RSCB parameterizations are notable, and in between, positive and negative biases come after each other. The ERSDs for  $\mu_r = 1$  more resemble the ERSD of the bin-based solver, as the biases for the number concentrations of the largest and smallest raindrops are substantially reduced. This shows that a proper choice of  $\mu_r$  may alleviate the deviation of the raindrop size distributions calculated by the RSCB parameterizations from the numerical solution, which is caused by the fixed shape of raindrop size distributions in bulk microphysics schemes.

The evolution of  $D_{m,r}$  for each simulation is presented in Fig. 4. For a fixed  $\mu_r$ , each RSCB parameterization has its own equilibrium diameter, which does not change with the initial  $D_{m,r}$ . For the initial  $D_{m,r}$  smaller than the equilibrium diameter,  $D_{m,r}$  increases up to the equilibrium diameter due to the self-collection process having a greater effect than the collisional breakup process. In contrast, for the initial  $D_{m,r}$  larger than the equilibrium diameter,  $D_{m,r}$  decreases down to the equilibrium diameter under a greater influence of the collisional breakup process.

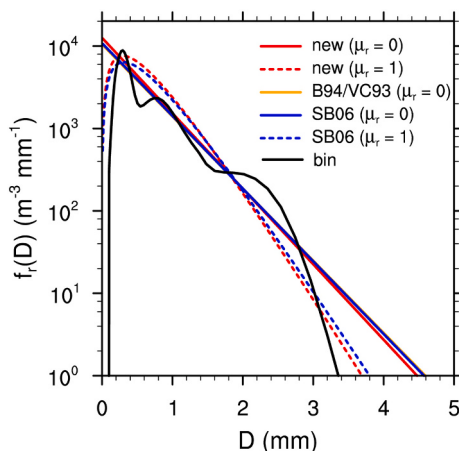


**Fig. 3.** The equilibrium drop size distribution in the box model simulations using the new, B94/VC93, and SB06 RSCB parameterizations and the bin-based solver of Seifert et al. (2005). Two different shape parameters ( $\mu_r = 0$  and  $\mu_r = 1$ ) are applied for the new and SB06 RSCB parameterizations.

When  $\mu_r = 0$ , the equilibrium diameter for the new RSCB parameterization (1.90 mm) is slightly smaller than the equilibrium diameters for the B94/V93 and SB06 RSCB parameterizations (1.99 mm for both). When  $\mu_r = 1$ , the equilibrium diameter for the new RSCB parameterization (1.49 mm) is also smaller than that for the SB06 RSCB parameterization (1.56 mm). The smaller equilibrium diameter in the new RSCB parameterization is expected to reduce the mean raindrop diameter if it replaces the RSCB parameterization in a bulk cloud microphysics scheme, for some simulations where RSCB is important. The equilibrium diameter for the bin-based solver is 1.20 mm, which is smaller than the equilibrium diameters for all of the RSCB parameterizations. This can be attributed to the different shape of ERSD of the bin-based solver, where the number concentration of large raindrops ( $D > \sim 3.1 \text{ mm}$ ) is lower than those in the ERSDs of the RSCB parameterizations. The equilibrium diameter for the new RSCB parameterization for  $\mu_r = 1$  is closest to that for the bin-based solver.

Besides the equilibrium diameter itself, the time required to reach the equilibrium diameter is also important because it is directly related to the RSCB rate. The two previous RSCB parameterizations that have the same equilibrium diameters show very different predictions from each other. For the initial  $D_{m,r}$  of 0.5 mm, it takes 9 min for the B94/V93 RSCB parameterization, and 51 min (45 min) for the SB06 RSCB parameterization when  $\mu_r = 0$  ( $\mu_r = 1$ ) to reach the equilibrium diameter. For the new RSCB parameterization, this time is 19 min (20 min) when  $\mu_r = 0$  ( $\mu_r = 1$ ), meaning smaller RSCB rates than those in the B94/V93 RSCB parameterization and larger RSCB rates than those in the SB06 RSCB parameterization, in the self-collection dominant regime. This time is 18 min for the bin-based solver, which is close to the prediction of the new RSCB parameterization. For the initial  $D_{m,r}$  of 3 mm, the time required to reach the equilibrium diameter is 12 min (14 min) in the new RSCB parameterization when  $\mu_r = 0$  ( $\mu_r = 1$ ), which is also intermediate between those in the B94/V93 (5 min) and SB06 (21 min for  $\mu_r = 0$  and 20 min for  $\mu_r = 1$ ). Compared to the abrupt decrease in  $D_{m,r}$  predicted by the B94/V93 RSCB parameterization, the new RSCB parameterization predicts relatively gradual decrease in  $D_{m,r}$  by the collisional breakup process. For the bin-based solver, it takes longer time (32 min) to reach the equilibrium diameter compared to the three RSCB parameterizations, and the SB06 RSCB parameterization yields the closest prediction to the bin-based solver.

The changes in  $D_{m,r}$  via RSCB are expected to affect various cloud microphysical process rates such as the accretion, evaporation, and sedimentation rates. In particular, for a given rainwater mass content, the precipitation rate increases as  $D_{m,r}$  becomes larger in the self-collection dominant regime and it decreases as  $D_{m,r}$  becomes smaller in the collisional breakup dominant regime.

#### 4. Simulations of shallow convective clouds

##### 4.1. Model setup

The developed scheme is first evaluated through large-eddy simulations (LES) of shallow convective clouds based on the data from the Rain in Cumulus over the Ocean (RICO) field campaign (Rauber et al., 2007). The RICO case has been simulated by various LES models (e.g., vanZanten et al., 2011; Kogan, 2013; Hoffmann et al., 2017; Kogan and Ovchinnikov, 2020), which makes it appropriate for the evaluation of a newly developed scheme by providing a plenty of previous simulation results to compare with. The initial and forcing data used in the simulations in this study are from the average conditions over the period from 16 December 2004 to 8 January 2005 during which mean precipitation rate was estimated to be a little less than  $1 \text{ mm d}^{-1}$ , as given in vanZanten et al. (2011). For the LES simulations, the new scheme is implemented into the Weather Research and Forecasting (WRF) model, version 4.2 (Skamarock et al., 2008). Yamaguchi and Feingold (2012) configured the LES mode of the WRF model for the RICO case by specifying the surface flux and large-scale forcing as described in vanZanten

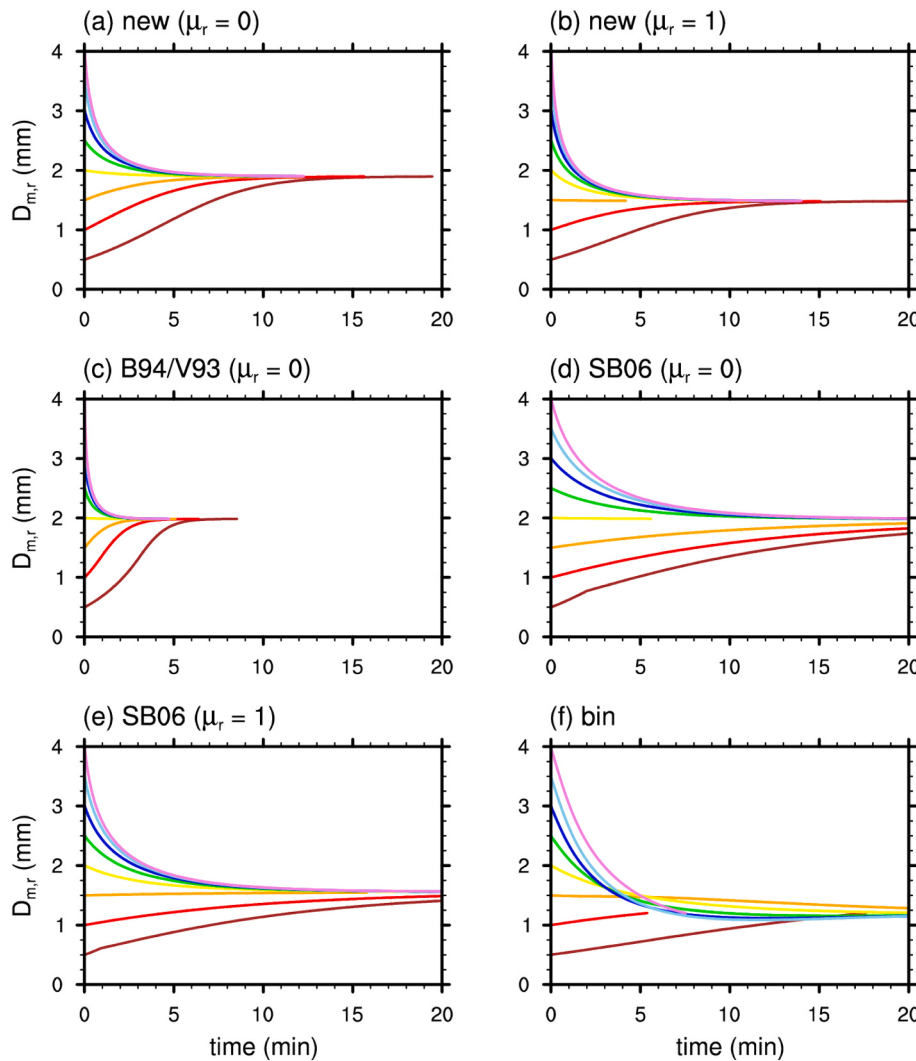


**Fig. 4.** Time series of the mass-weighted mean diameter of raindrops in the box model simulations using the (a) new RSCB parameterization with  $\mu_r = 0$  and (b) with  $\mu_r = 1$ , (c) B94/VC93 RSCB parameterization, (d) SB06 RSCB parameterization with  $\mu_r = 0$  and (e) with  $\mu_r = 1$ , and (f) bin-based solver of Seifert et al. (2005). Eight different initial mass-weighted mean diameters ranging from 0.5 to 4 mm with 0.5-mm intervals are tested and represented by different colors. The initial rainwater mass content is fixed to  $2 \text{ g m}^{-3}$ .

et al. (2011). In this study, this configuration is applied to the version 4.2 of the WRF model.

In this configuration, grid spacing is horizontally 100 m and vertically  $\sim 40$  m, and the domain size is  $12.8 \times 12.8$  km in the horizontal and 4 km in the vertical with periodic lateral boundary conditions. The sea surface temperature is fixed to 299.8 K. The surface heat, moisture, and momentum fluxes are computed using the near-surface and surface values, and the large-scale subsidence and the thermodynamic forcing that includes radiative forcing are prescribed. More detailed information is given in vanZanten et al. (2011) and Yamaguchi and Feingold (2012). The initial profiles of thermodynamic variables and horizontal winds are given in Fig. 5. Convections are initiated after the initial random perturbations on the potential temperature and water vapor mixing ratio fields, which are  $[-0.1, 0.1 \text{ K}]$  and  $[-0.025, 0.025 \text{ g kg}^{-1}]$ , respectively. The time step is 0.25 s. The model is integrated for 24 h, and the simulation data from the last 12 h of the simulations are used for the analysis in this study, except for the time-series analysis. The CCN properties in the cloud microphysics scheme are also set exactly as given in vanZanten et al. (2011), assuming a bimodal CCN spectrum where the total CCN concentration for the two modes are 90 and  $15 \text{ cm}^{-3}$ , respectively.

#### 4.2. Other collection/breakup parameterizations

To evaluate the effects of the sophisticated and physically based

warm-cloud collection and breakup parameterizations, some previous collection parameterizations are also tested in the same framework. In additional simulations with the same model setup, the autoconversion (including the self-collection of cloud droplets), accretion, and RSCB parameterizations in the new scheme are replaced with the warm-cloud collection (and breakup if available) parameterizations of K13 and SB06. The parameterizations of other microphysical processes remain the same. Below are the brief descriptions for the K13 and SB06 parameterizations.

The K13 parameterizations are simple and computationally efficient parameterizations where the autoconversion, accretion, and raindrop self-collection rates are expressed as power-law equations. The coefficients in the power-law equations were obtained by fitting to the shallow cumulus simulation data of an LES model with a bin micro-physics scheme. Although the parameterizations of Kharoutdinov and Kogan (2000) which were obtained using the same method but based on the simulations of marine boundary layer stratocumulus clouds are widely used in bulk schemes, the K13 parameterizations developed for shallow cumulus clouds are chosen for comparison because they are thought to be more suitable for the simulations in this study. The raindrop collisional breakup process is not considered in the K13 parameterizations, which may be acceptable for the simulation of shallow convective clouds where the raindrop self-collection process is expected to be more active compared to the raindrop collisional breakup process.

The SB06 parameterizations have analytic forms that were derived

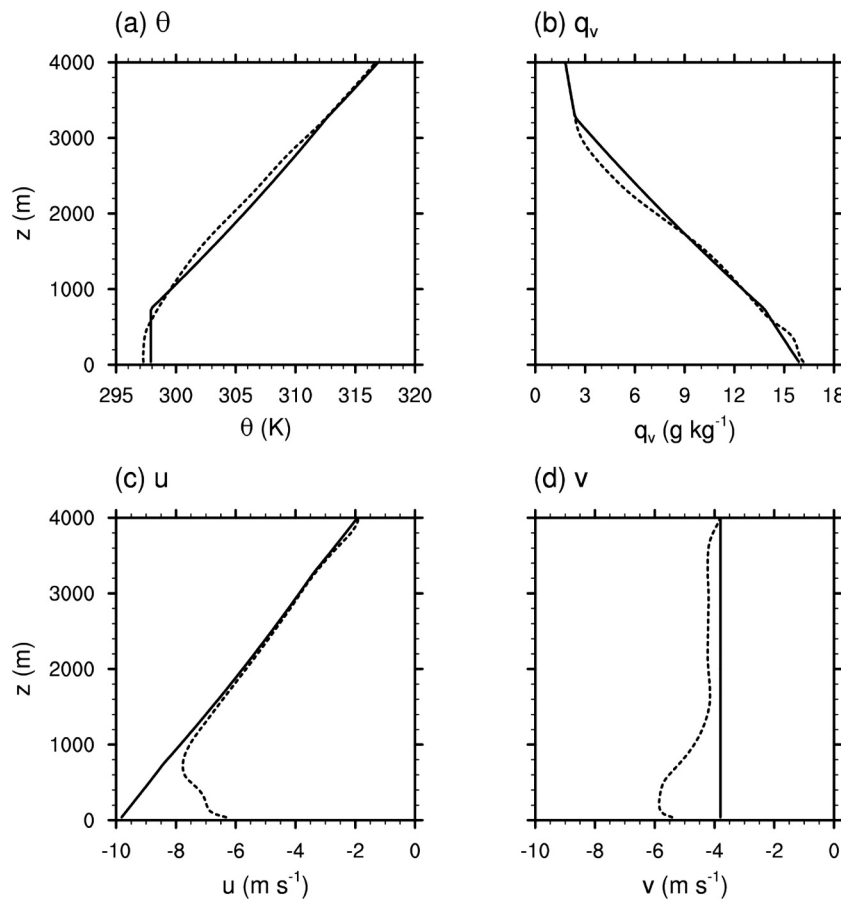


**Fig. 5.** Vertical profiles of (a) potential temperature  $\theta$ , (b) water vapor mixing ratio  $q_v$ , and horizontal winds (c)  $u$  and (d)  $v$  at initial state (solid lines) and those averaged over the last 12 h of the simulation with the new collection and breakup parameterizations (dashed lines).

from the SCE with an approximate collection kernel. In addition, each SB06 parameterization includes a correction term obtained by fitting to the numerical solution of the SCE. The correction terms for the auto-conversion and accretion parameterizations are given as a function of the proportion of the rainwater mass content to the total liquid water mass content,  $L_r/(L_c + L_r)$  where  $L$  is the hydrometeor mass content, referred to as the internal time scale. Both raindrop self-collection and collisional breakup processes are considered in the SB06 parameterizations, as described in subsection 2.2. Hereafter, the bulk schemes with the warm-cloud collection (and breakup) parameterizations of K13 and SB06 used in the two additional simulations, respectively, are simply called K13 and SB06 for brevity.

#### 4.3. Simulation results

The simulation with the new scheme predicts the 24-h accumulated precipitation amount of  $\sim 0.8$  mm (Fig. 6a), which agrees well with the radar-estimated average precipitation rate in the target period, a little less than  $1 \text{ mm d}^{-1}$  (vanZanten et al., 2011). The overall values and time series of the liquid water path, rainwater path, and cloud cover simulated with the new scheme are comparable to those of the simulations using various models and cloud microphysics schemes in vanZanten et al. (2011) (Fig. 6c–e). The last 12-h averaged cloud cover is 0.21, which is also comparable to an airborne lidar-based estimate (0.17) (Nuijens et al., 2009). Compared to the new scheme, K13 predicts 41% larger accumulated precipitation amount. The liquid water path, rainwater path, and cloud cover averaged over the last 12 h of the simulation are 21% smaller, 33% larger, and 57% smaller, respectively, than those predicted by the new scheme. These show that K13 predicts higher efficiency of precipitation formation and heavier precipitation than the

new scheme. Considering the big differences between the predictions of the new scheme and K13, SB06 gives somewhat similar predictions to the new scheme. The 24-h precipitation amount and the last 12-h averaged liquid water path predicted by SB06 and the new schemes are very close to each other; they deviate by no more than 4% from each other. However, the new scheme shows 14% smaller rainwater path and 13% larger cloud cover than SB06. Through additional simulations, it is found that these differences do not change much by a slight perturbation on the initial condition. Although the microphysics–radiation feedback is not considered in these simulations, the larger horizontal extent of cumulus clouds in the new scheme is expected to affect the radiation (e.g., more reflection of solar radiation and thus cooling of low atmosphere in the daytime) when it is implemented into weather and climate models.

The vertical profiles of the last 12-h averaged hydrometeor mass mixing ratios and number concentrations are presented in Fig. 7. In the new scheme, the averaged liquid water mass mixing ratio greater than  $10^{-4} \text{ g kg}^{-1}$  exists up to  $z = 2960 \text{ m}$ . The cloud water and rainwater mass mixing ratios peak at  $z = 680$  and  $800 \text{ m}$ , respectively, slightly above the cloud base, and decrease until the cloud top (Fig. 7a and b). The mean cloud droplet number concentration is generally  $\sim 50\text{--}65 \text{ cm}^{-3}$  (at  $z = 720\text{--}2160 \text{ m}$ ) as intended by the CCN specifications, and it is smaller at the levels near the cloud base and cloud top (Fig. 7c). The mean raindrop number concentration in the new scheme gradually increases from the surface ( $1.4 \times 10^{-3} \text{ cm}^{-3}$ ) to  $z = 1320 \text{ m}$  ( $4.4 \times 10^{-3} \text{ cm}^{-3}$ ) (Fig. 7d), partly satisfying the observational constraints that were not satisfied in the LES simulations in vanZanten et al. (2011).

Unlike the new scheme and SB06 which predict overall greater amounts of cloud water mass than rainwater mass above the cloud base, K13 predicts an overall greater amount of rainwater mass than cloud

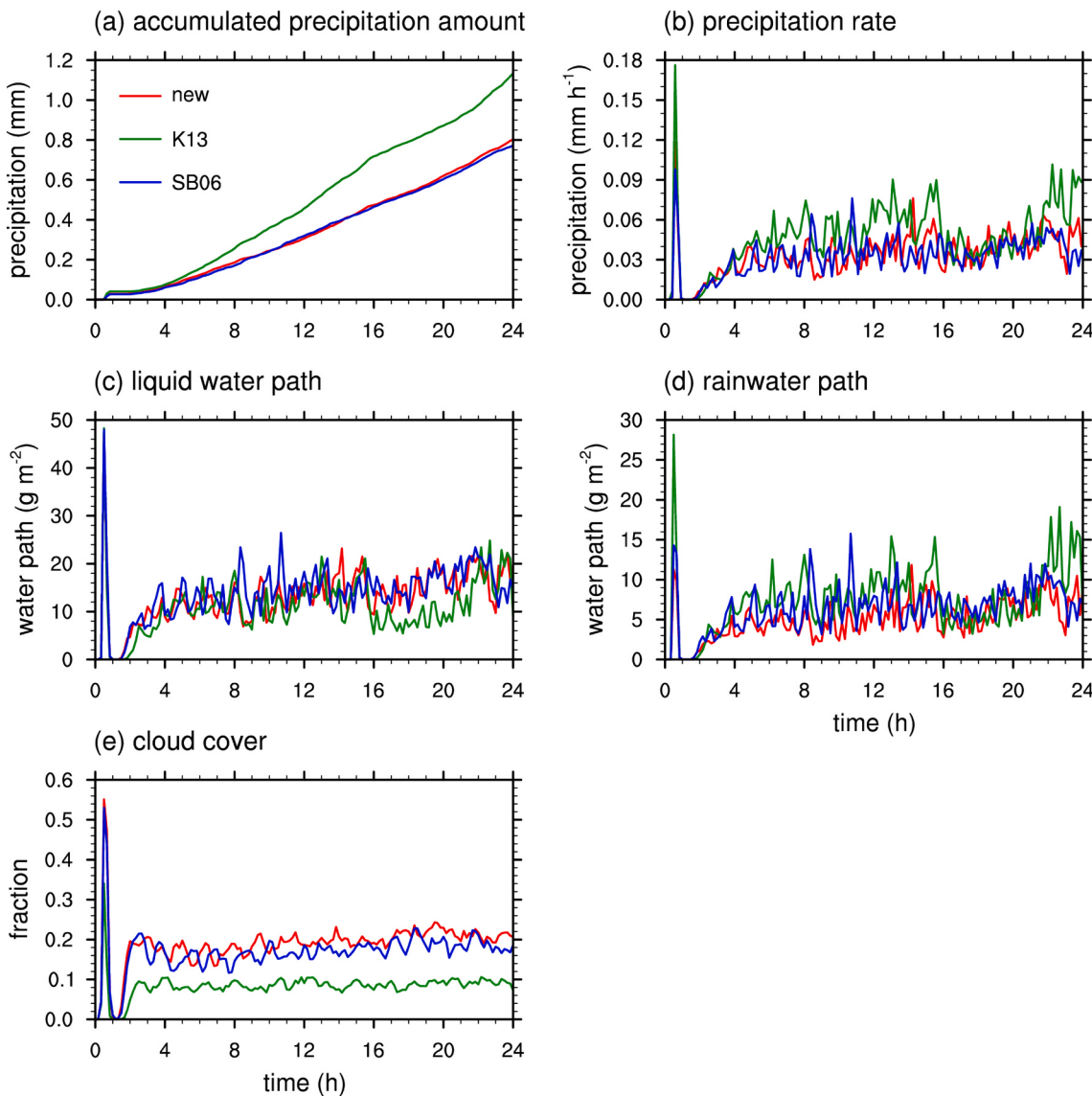


**Fig. 6.** Time series of domain-averaged (a) accumulated precipitation amount, (b) precipitation rate, (c) liquid water path, (d) rainwater path, and (e) cloud cover (fraction of cloudy columns where at least one grid with the cloud water mixing ratio greater than  $0.01 \text{ g kg}^{-1}$  exists) in the simulations with different collection and breakup parameterizations.

water mass, indicating relatively efficient conversion from cloud water to rainwater. Although the amount of cloud water mass is relatively small, the mean cloud droplet number concentration is relatively high in K13, leading to a smaller mean size of cloud droplets. K13 shows abrupt changes in the mean raindrop number concentration at low levels with its sudden peak at  $z = 240 \text{ m}$ , which is hardly acceptable. Compared to SB06, the new scheme shows a larger amount of cloud water mass in most part of the clouds ( $z \geq 640 \text{ m}$ ) and a noticeably smaller amount of rainwater mass. The reason for the smaller amount of rainwater mass in the new scheme than in SB06 despite the similar precipitation amounts is faster sedimentation of raindrops whose mean size is larger in the new scheme, which can be inferred from the much lower mean raindrop number concentration in the new scheme. In addition, SB06 predicts a relatively sharp increase in the mean raindrop number concentration with height compared to the new scheme.

The different profiles of hydrometeor mass mixing ratios and number concentrations result from the different microphysical process rates in the three schemes. Fig. 8 shows the last 12-h averaged mass conversion rates through the autoconversion, accretion, condensation, and evaporation processes. In these shallow convective cloud simulations, the

autoconversion process is the most important source of rainwater mass, followed by the accretion process. Overall, the new scheme shows the smallest autoconversion rates among the three schemes (Fig. 8a). The less depletion of the cloud water by autoconversion in the new scheme leads to the larger amount of cloud water mass (Fig. 7a), which can enhance the accretion, condensation (onto cloud droplets), and cloud droplet evaporation processes that depend on the cloud water mass (Fig. 8b-d). The raindrop evaporation process is the least active in the new scheme (Fig. 8e), possibly due to the small amount of rainwater mass, large mean raindrop size, and resultant fast sedimentation. K13 predicts that the maximum autoconversion rate takes place at a very low level ( $z = 400 \text{ m}$ ), just above the cloud base (Fig. 8a). This causes the peak of rainwater mass to be located at the low level (Fig. 7b) and generate the spurious peak of the mean raindrop number concentration at the low level (Fig. 7d). The large amount of small raindrops at the low levels produced by the autoconversion process results in the large rates of raindrop evaporation at the lowest levels.

The production rates of raindrop number concentration by the autoconversion process in the new scheme are much smaller compared to those in the other schemes, and their ratios to the autoconversion

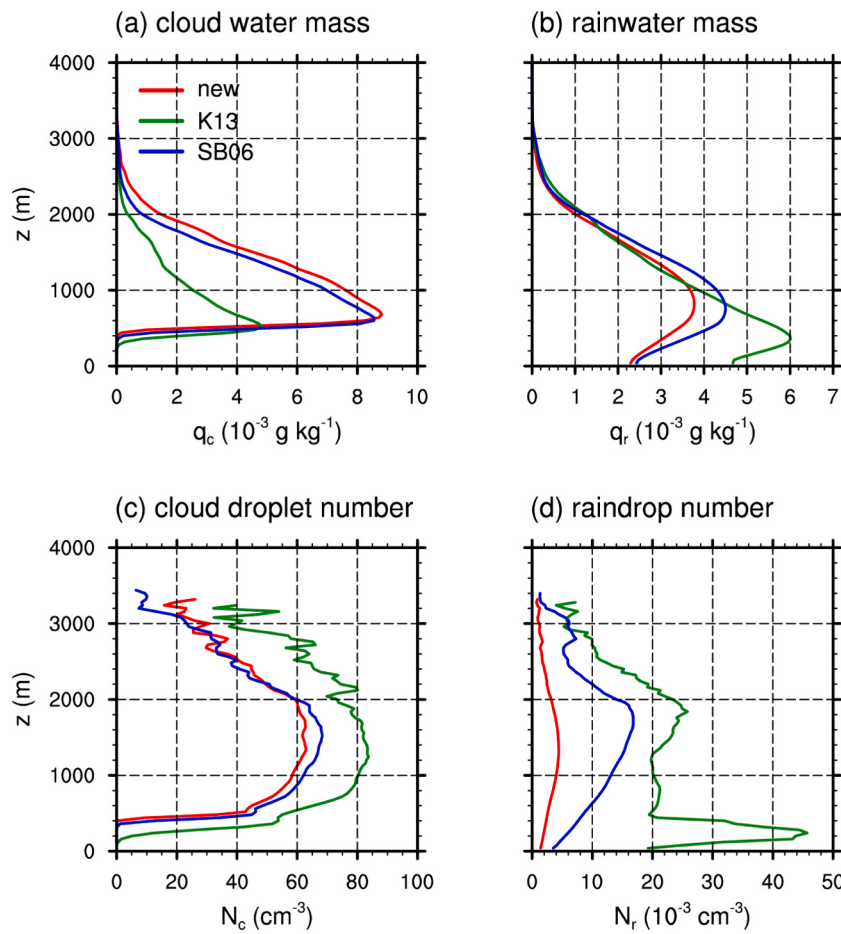


**Fig. 7.** Vertical profiles of horizontally averaged (a) cloud water mass mixing ratio, (b) rainwater mass mixing ratio, (c) cloud droplet number concentration, and (d) raindrop number concentration averaged over the last 12 h of the simulations with different collection and breakup parameterizations. Note that the horizontal average of the cloud droplet (raindrop) number concentration is computed by weighted averaging where the cloud droplet mass mixing ratio is used as the weight.

(mass conversion) rates are also relatively small (Figs. 8a and 9a). The K13 and SB06 autoconversion parameterizations simply calculate the raindrop number production rate by dividing the autoconversion (mass conversion) rate by the mass of a raindrop with a specified size. The substantially smaller ratios of number production rates to mass conversion rates in the new scheme indicate that some raindrops larger than the raindrop with the specified size are also produced as a result of the autoconversion process. This suggests that two-moment bulk schemes need to explicitly parameterize the raindrop number production rate as the new scheme does. The small rates of raindrop number production by the autoconversion process are the reason for the low mean raindrop number concentration in the new scheme (Fig. 7d), which coincides with the aircraft observation (vanZanten et al., 2011). Compared to the autoconversion, RSCB does not play an important role in these shallow convective cloud simulations. The raindrop number depletion rates by RSCB are about 2-order smaller than the raindrop number production rates by the autoconversion process (Fig. 9a and b). The depletion rates are the smallest in the new scheme, but this seems to be caused by the low mean raindrop number concentration mainly affected by the autoconversion process.

The characteristics of individual parameterizations in the three schemes are further examined by roughly removing the major dependencies of each parameterization on corresponding hydrometeor mass content or number concentration. Each microphysical process rate

is normalized, and its PDF is plotted (Fig. 10). The normalized autoconversion rate shows the biggest discrepancies between the three schemes so that the  $x$ -axis is expressed in log scale (Fig. 10a). The normalized autoconversion rates in the new scheme are least dispersed, meaning that the autoconversion rates in the new scheme have relatively high dependency on  $L_c^2$  in these simulations with well-constrained  $N_c$ . In contrast, the normalized autoconversion rates in K13 are extremely dispersed, with their largest values that are  $\sim 10^5$  times the largest values in the new scheme. This can be attributed to the use of a simple power-law equation to express the autoconversion rate, which can give too large values for certain conditions. The large autoconversion rates near the cloud base in K13 (Fig. 8a) seem to be related to this characteristic. The normalized accretion rates in the new scheme show the broadest distribution (Fig. 10b). As argued in A20, the accretion rate should depend not only on  $L_c$  and  $L_r$  but also on  $N_c$  and  $N_r$ , which justifies the relatively wide distribution in the new scheme. On the other hand, SB06 shows the narrowest distribution of normalized accretion rates because the accretion rates in this scheme are too highly dependent on the mass contents.

In the PDF of the normalized RSCB rates, the new scheme shows one peak for the self-collection dominant regime (negative RSCB rates) and another peak for the collisional breakup dominant regime (positive RSCB rates) (Fig. 10c). The positive RSCB rates mainly appear in the lower portion of clouds and below the cloud base where the mean

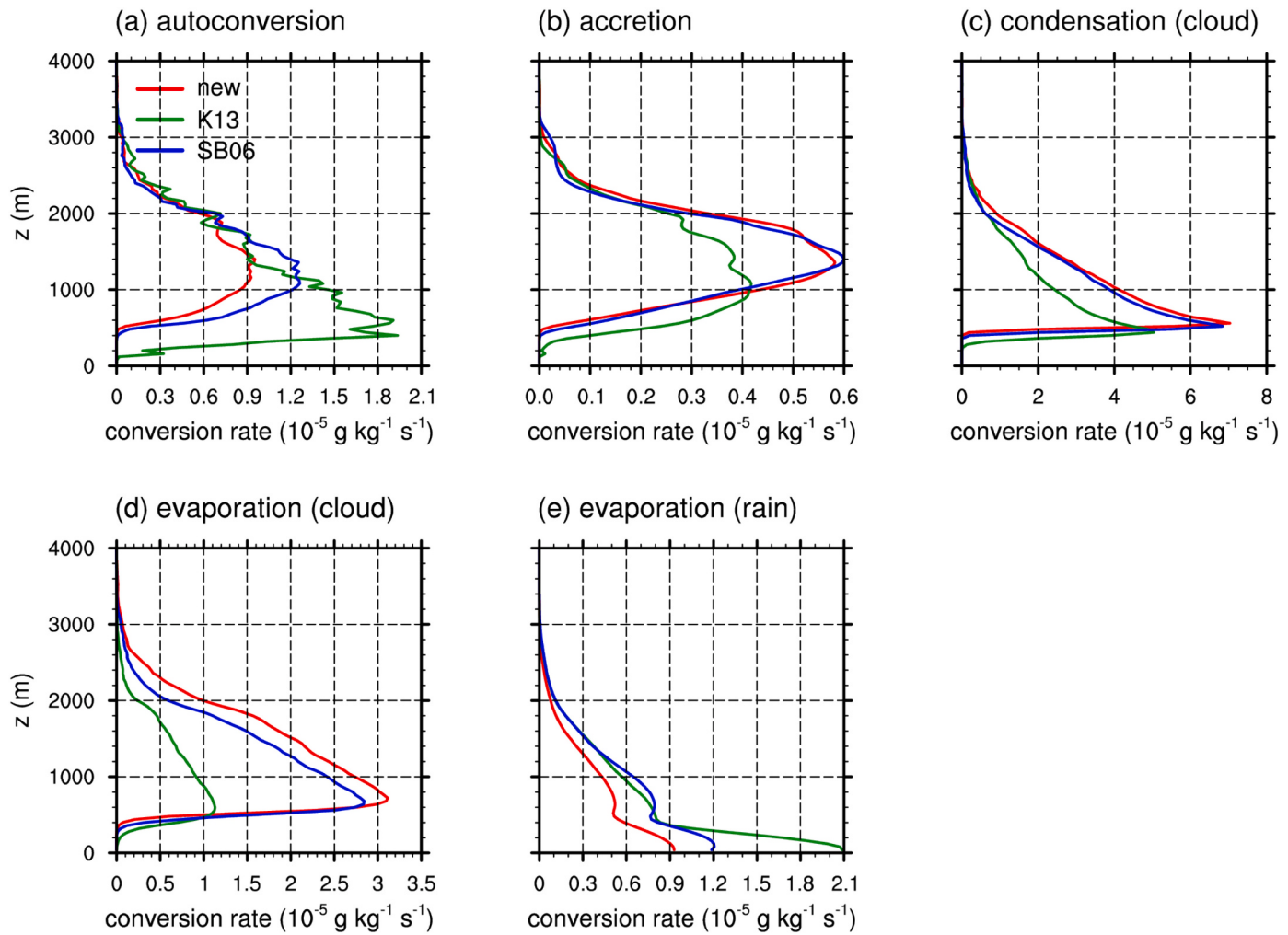


**Fig. 8.** Vertical profiles of horizontally averaged mass conversion rates via the (a) autoconversion, (b) accretion, (c) condensation to cloud water, (d) evaporation of cloud water, and (e) evaporation of rainwater averaged over the last 12 h of the simulations with different collection and breakup parameterizations.

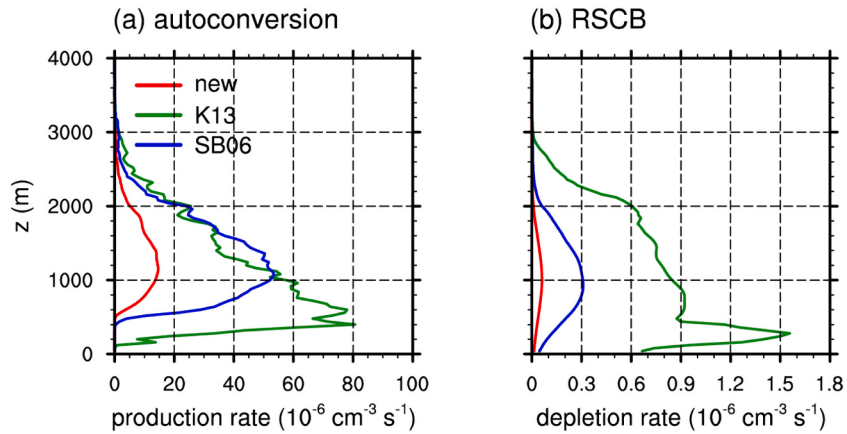


**Fig. 9.** Vertical profiles of horizontally averaged raindrop number change rates via (a) the autoconversion and (b) RSCB averaged over the last 12 h of the simulations with different collection and breakup parameterizations.

raindrop diameter is relatively large (not shown). K13 shows the broadest distribution of the normalized RSCB rates which can also be attributed to the use of a simple power-law equation. It is noteworthy that some positive RSCB rates are predicted even in these shallow convective cloud simulations by the new scheme and SB06, while these cannot be represented in K13 where the collisional breakup

parameterization is not included. Compared to SB06, the peak for the self-collection dominant regime in the new scheme is shifted toward the less negative direction, and the peak for the collisional breakup dominant regime is shifted toward the more positive direction.

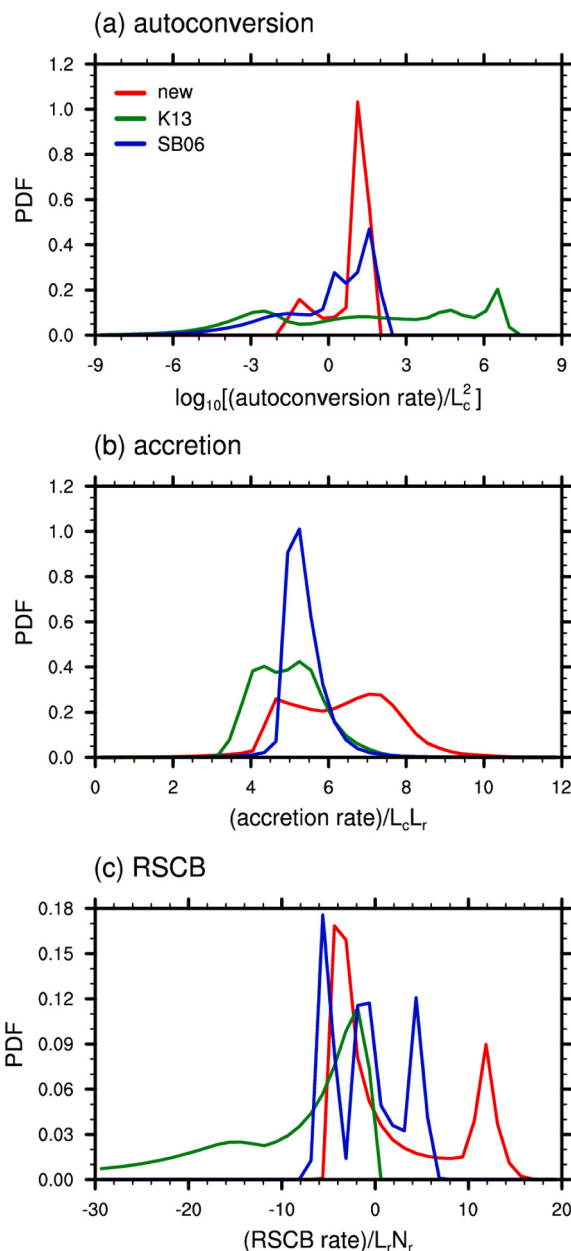


**Fig. 10.** Probability density function (PDF) for normalized (a) autoconversion, (b) accretion, and (c) RSCB rates in the last 12 h of the simulations with different collection and breakup parameterizations. Note that only non-zero values of the microphysical process rates are considered in the PDFs.

## 5. Simulations of a convective cloud with a large liquid water path

### 5.1. Model setup

In addition to the simulations of the RICO case presented above, an idealized single convective cloud is simulated using the three different bulk schemes. Compared to the clouds in the RICO case, this cloud is more convective with a higher cloud top and a larger liquid water path so that RSCB may play a bigger role. The WRF model version 4.2 is also used for this case, but no surface flux and large-scale forcing are considered. The domain size and grid spacing are  $25 \times 25$  km and 250 m in the horizontal and 8 km and  $\sim 100$  m in the vertical, respectively. Open lateral boundary conditions are applied. The model time step is 2 s, and the model is integrated for 1 h. Note that only the simulation results

within the  $8 \times 8$  km area centered at the domain center is used for analysis because almost no hydrometeor exists outside this area.

The initial profiles of potential temperature  $\theta$  and water vapor mixing ratio  $q_v$  are given by

$$\theta(z) = \begin{cases} \theta_0 + (\theta_1 - \theta_0) \left( \frac{z}{z_1} \right)^{8/5}, & z \leq z_1 \\ \theta_1 + (\theta_2 - \theta_1) \left( \frac{z - z_1}{z_2 - z_1} \right), & z > z_1 \end{cases} \quad (17)$$

$$q_v(z) = \begin{cases} q_{v,0} \left[ 1 - \left( \frac{z}{z_2} \right)^{7/8} \right], & z \leq z_2 \\ 0, & z > z_2 \end{cases} \quad (18)$$

where  $z_1 = 6$  km,  $z_2 = 8$  km (domain top),  $\theta_0 = 300$  K,  $\theta_1 = 333$  K,  $\theta_2 = 350$  K, and  $q_{v,0} = 16$  g kg<sup>-1</sup>. The expression forms in Eqs. (17) and (18) are similar to those for the initial profiles of Weisman and Klemp (1982) which are designed to trigger deep convection, but different coefficients are applied to prevent the cloud from growing vertically too much above the freezing level. These initial profiles are tested using the WRF double-moment 6-class scheme (Lim and Hong, 2010) where both liquid and ice microphysics are considered and only negligible amounts of ice hydrometeors are generated (not shown). This indicates that it is appropriate to use these profiles to evaluate the warm-cloud microphysics schemes in a liquid-only framework.

To evaluate the performance of the bulk schemes, a warm version of the Hebrew University Cloud Model (HUCM) bin microphysics scheme (Khain et al., 2011) is coupled with the WRF model as a reference. Note that the bin scheme employs the collisional breakup parameterization of Seifert et al. (2005) which is used to develop the new RSCB parameterization in this study.

### 5.2. Simulation results

In these single cloud simulations, the precipitation rate, liquid water path, and rainwater path are more than 1-order greater than those in the RICO case simulations presented in Section 4, mainly due to the stronger convective activity induced by the vertically more unstable initial condition. The peak time of precipitation rate predicted by the new scheme ( $t \sim 23$  min) coincides with that predicted by the bin scheme, and it is 2 min later than that in K13 and 4 min earlier than that in SB06 (Fig. 11b). The 1-h accumulated precipitation amount in the new scheme is 0.37 mm, which is smaller than that in the bin scheme (0.43 mm) and K13 (0.49 mm) and larger than that in SB06 (0.29 mm) (Fig. 11a). The time evolutions of liquid water path and rainwater path in the new scheme are very similar to those in the bin scheme until  $t = 20$  min (Fig. 11c and d). These similarities show the superiority of the new scheme for the prediction of precipitation onset. The precipitation rate at the first peak in the new scheme is 36% larger than that in the bin scheme although the rainwater mass produced until this time is similar in the two schemes. This may be attributed to the deviation of raindrop size distribution in the bin scheme from the prescribed gamma size distribution in the new scheme, which can induce the difference in the sedimentation process. Unlike in the shallow cumuli field simulations in Section 4 where the new scheme and SB06 relatively well agree for the precipitation amount, the two schemes show significantly different time series of precipitation amount and rate in the single cloud simulations with a larger liquid water path.

The vertical profiles of cloud water and rainwater masses in the new scheme are also similar to those in the bin scheme, especially in terms of the maximum amounts of cloud water mass (overestimated by 4%) and rainwater mass (underestimated by 8%) (Fig. 12a and b). On the other hand, compared to the bin scheme, K13 and SB06 predict much larger amounts of cloud water mass and much smaller amounts of rainwater mass, indicating that the conversion processes of cloud water mass into

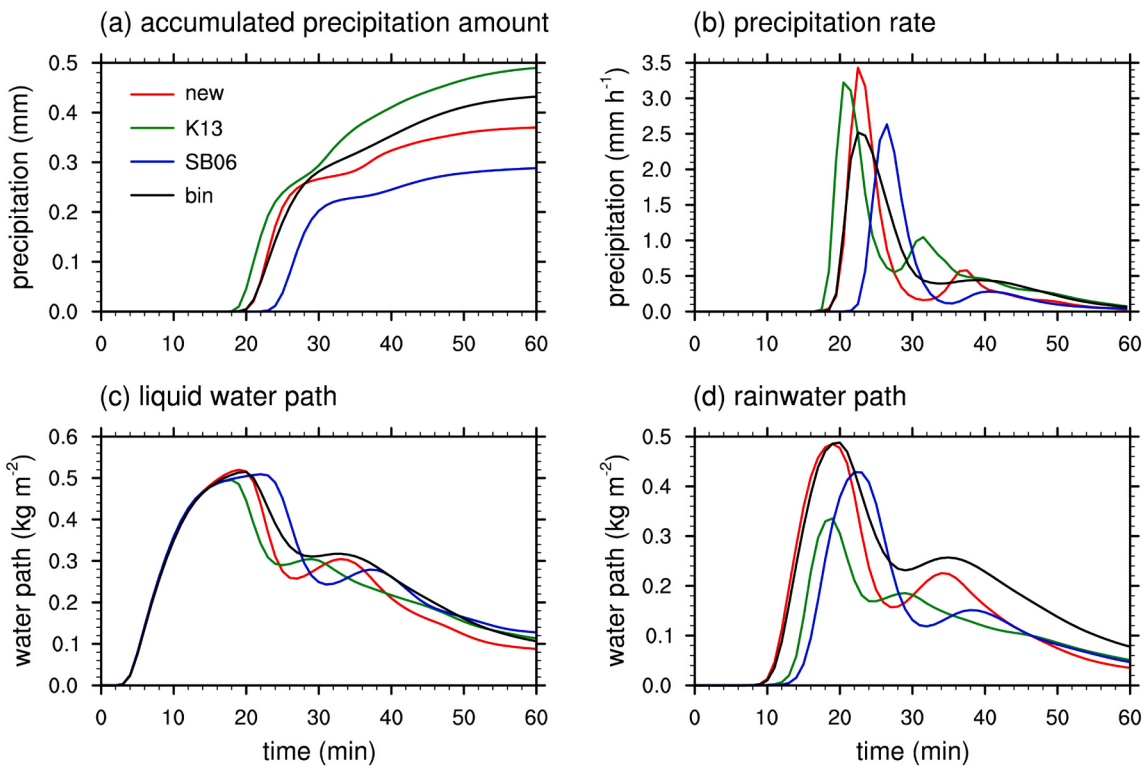


**Fig. 11.** Time series of area-averaged (a) accumulated precipitation amount, (b) precipitation rate, (c) liquid water path, and (d) rainwater path in the simulations with the bulk schemes with different collection and breakup parameterizations and the bin scheme.

rainwater mass are less effective in these two schemes.

All of the three bulk schemes show significantly higher cloud droplet number concentrations than the bin scheme (Fig. 12c). The main reason for this discrepancy is the difference in the representation of CCN number concentration between the bulk schemes and the bin scheme. While the bin scheme prognoses the CCN size distribution so that the CCN number concentration is reduced due to the activation process and replenished gradually, the bulk schemes used in this study are designed to prescribe the CCN size distribution which is unchanged during the model integration because of the difficulties and uncertainties in fully describing the sources and sinks of CCN number concentration. The assumption of fixed CCN number concentration in the bulk schemes can act as instant replenishment of CCN number concentration during the activation process. Therefore, if the newly produced cloud droplets via the CCN activation are rapidly transported upward due to strong convection as in this case, a large number of CCN is activated immediately again, increasing the cloud droplet number concentration. Despite the large discrepancy in the cloud droplet number concentration, the raindrop number concentrations in the three bulk schemes are comparable with that in the bin scheme (Fig. 12d). Compared to the other bulk schemes, the new scheme predicts overall a higher raindrop number concentration.

Unlike in the RICO case simulations, RSCB plays a major role in the changes in raindrop number concentration in these single cloud simulations. The raindrop number depletion rate by RSCB is comparable to the raindrop number production rate by the autoconversion process (Fig. 13). The new scheme shows the largest raindrop number depletion rate by RSCB among the three bulk schemes, and it is close to that in the bin scheme. The new scheme predicts much larger raindrop number production rate by the autoconversion process compared to the bin scheme and the other bulk schemes. Because the cloud droplet number concentrations in the bulk schemes and the bin scheme are too different from each other, it is difficult to evaluate the performance of each bulk scheme for the prediction of the raindrop number production rate by the

autoconversion process that deeply depends on the cloud droplet number concentration.

The PDFs of the normalized microphysical process rates are presented in Fig. 14. It is noteworthy that the PDF patterns of the normalized microphysical process rates in the single cloud simulations are similar to those in the RICO case simulations although the cloud and precipitation characteristics are totally different in the two sets of simulations. For the normalized autoconversion rates, the new scheme shows the most concentrated distribution among the three bulk schemes, which is also shown by the bin scheme. The highest peak in the new scheme is shifted to the left compared to that in the bin scheme, possibly due to the difference in the cloud droplet number concentration. For the normalized accretion rates, the new scheme shows the most dispersed distribution, which is not consistent with the bin scheme that shows a concentrated distribution. The reason for the wide distribution of the normalized accretion rates in the new scheme is its dependency on the number concentrations of cloud droplets and raindrops which are simulated to be highly variable with height by the bulk schemes. The PDF of the normalized RSCB rates in the bin scheme has a high single peak in the self-collection dominant regime, as in the new scheme.

The parameterizations in the new scheme are derived by using elaborate representations of collection and breakup kernels in the SCE and SBE, which leads to the advantages of the new scheme in predicting cloud and precipitation properties. These elaborate representations complicate the parameterization form and extends the computation time to some extent. For the single cloud simulations in this section, the computation time of the simulation with the new scheme is about twice that for K13. The computation time for the new scheme is 4.4 times shorter than that for the bin scheme. This indicates that the new scheme retains the advantage of a bulk scheme over a bin scheme in terms of computational cost. Moreover, the relative difference in computation time between the new scheme and K13 is expected to be substantially reduced when it is applied in operational models where many types of physics parameterization schemes (e.g., shortwave/longwave radiation

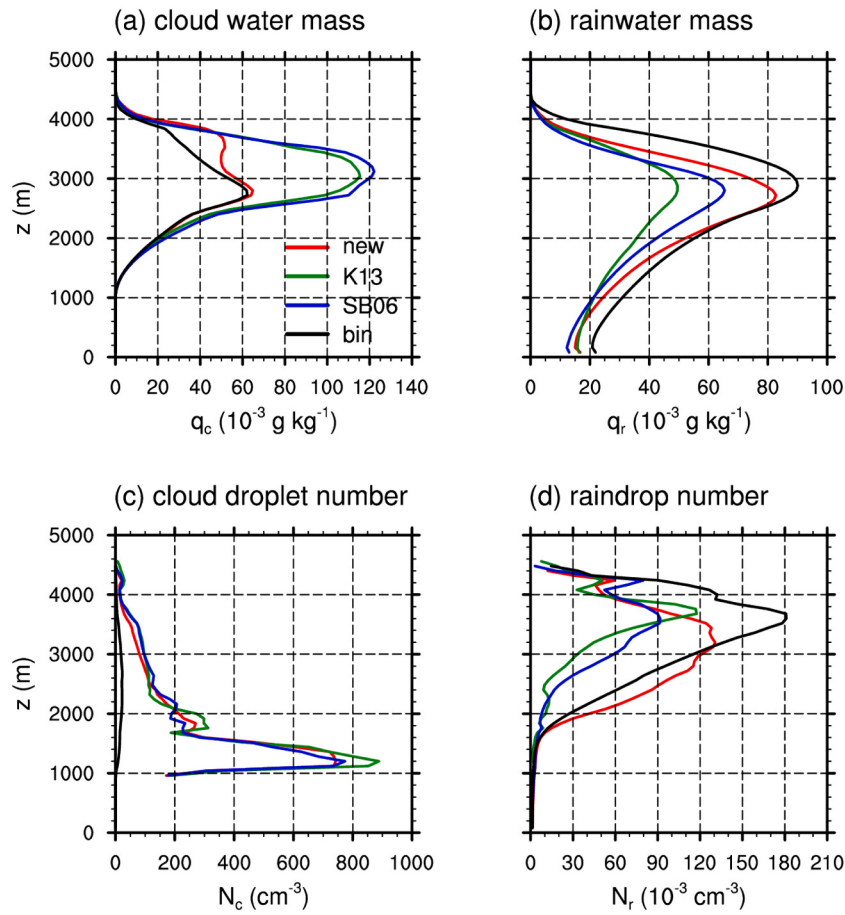


**Fig. 12.** Vertical profiles of horizontally averaged (a) cloud water and (b) rainwater mass mixing ratios and (c) cloud droplet and (d) raindrop number concentrations averaged over the 1-h simulation period of the simulations with the bulk schemes with different collection and breakup parameterizations and the bin scheme. Note that the horizontal averages of the number concentrations are mass mixing ratio-weighted averages.

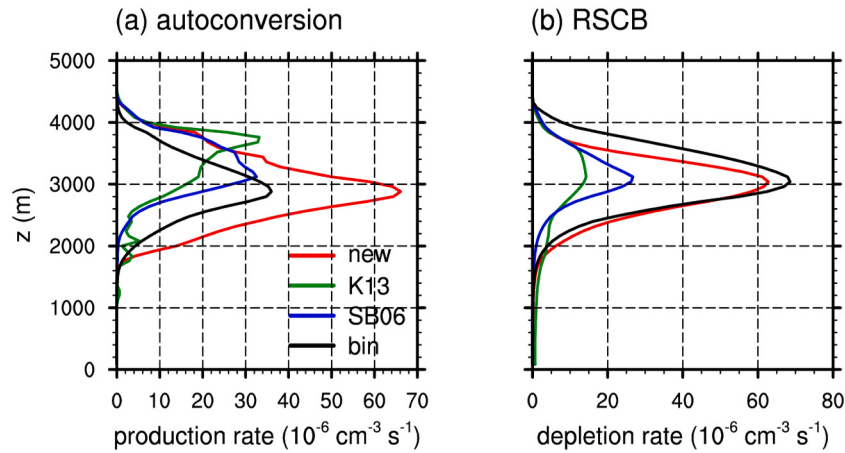


**Fig. 13.** Vertical profiles of horizontally averaged raindrop number change rates via (a) the autoconversion and (b) RSCB averaged over the 1-h simulation period of the simulations with the bulk schemes with different collection and breakup parameterizations and the bin scheme.

schemes, planetary boundary layer schemes, and land surface schemes) other than cloud microphysics schemes are also used.

## 6. Summary and conclusions

We developed a two-moment bulk microphysics scheme with warm-cloud collection and breakup parameterizations that were derived by approximating the collection and breakup kernels in the SCE and SBE

and analytically evaluating the integrals in these equations. The autoconversion parameterization was from LB17, and the accretion parameterization was from A20. The raindrop self-collection and collisional breakup (RSCB) parameterization was newly developed in this study, making use of the coalescence efficiency ( $\eta_{\text{coal}}$ ) and fragment drop number ( $\bar{N}_f$ ) parameterizations of Seifert et al. (2005). The developed RSCB parameterizations were evaluated using a box model and showed

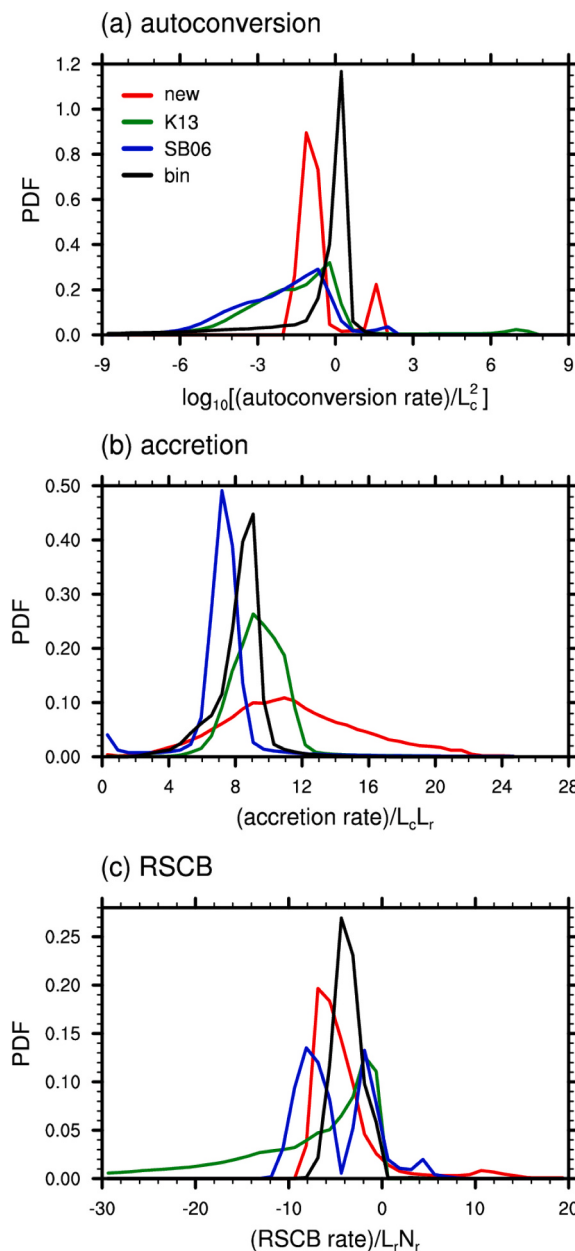


**Fig. 14.** Probability density function (PDF) for normalized (a) autoconversion, (b) accretion, and (c) RSCB rates in the simulations with the bulk schemes with different collection and breakup parameterizations and the bin scheme. Note that only non-zero values of the microphysical process rates are considered in the PDFs.

good agreement in the equilibrium raindrop size distribution with the bin-based solver when  $\mu_r = 1$ .

The developed scheme was evaluated through the idealized LES simulations of precipitating shallow convective clouds during the RICO field campaign. The precipitation amount, cloud cover, and mean cloud droplet and raindrop number concentrations predicted in the simulation using the new scheme agreed well with those observed during the field campaign. Compared to the relatively simple previous

parameterizations, the autoconversion parameterization in the new scheme yielded relatively small rainwater mass production rates. The ratios of raindrop number production rates to mass conversion rates via the autoconversion process were substantially smaller in the new scheme than in the previous schemes, due to the limitation of the simple representation of the raindrop number production rate in the previous schemes. The normalized accretion rates in the new scheme were most widely distributed, which shows the dependence of accretion rates in the new scheme on both masses and numbers of hydrometeors. These had great influence on the different cloud and precipitation properties between the simulations.

To evaluate the new scheme in an environment where RSCB plays a major role in the changes in raindrop number concentration, a single convective cloud with a large liquid water path was simulated. The performance of the new scheme was evaluated by comparison with a bin microphysics scheme. In these simulations, the time of precipitation onset, 1-h accumulated precipitation amount, time series of rainwater path predicted by the new scheme were close to those predicted by the bin microphysics scheme. The raindrop number depletion rate by RSCB predicted by the new scheme was also close to that predicted by the bin scheme.

One advantage of the parameterizations derived using the analytic approximation approach is that they are flexible to changes in the assumptions in the microphysics scheme. Our current knowledge of certain components crucial to microphysical processes is poor. For example, the coalescence efficiency between drops and the number of fragment drops produced by collision are highly uncertain so that even the bin scheme results do not agree with each other (Prat et al., 2012). These kinds of uncertainties can be reduced through observations, laboratory experiments, theoretical improvements, and particle-by-particle direct numerical simulations. Then, the parameterizations derived using the analytic approximation approach can be easily modified with improved representations of the important components in the governing equations which are, for collection and breakup processes, SCE and SBE. Also, the parameterizations can be easily extended to be used in three-moment bulk schemes which can be operationally used in the future, because these parameterizations describe the dependencies on all three parameters in the gamma size distribution.

#### CRediT authorship contribution statement

**Han-Gyul Jin:** Conceptualization, Methodology, Validation, Formal analysis, Investigation, Data curation, Writing – original draft, Visualization. **Jong-Jin Baik:** Conceptualization, Formal analysis, Investigation, Writing – review & editing, Supervision. **Hyunho Lee:** Conceptualization, Methodology, Formal analysis, Writing – review & editing. **Tanvir Ahmed:** Formal analysis, Writing – review & editing.

#### Declaration of Competing Interest

The authors declare that they have no known competing financial interests or personal relationships that could have appeared to influence the work reported in this paper.

#### Acknowledgements

The authors are grateful to two anonymous reviewers for providing valuable comments on this work. This work was supported by the National Research Foundation of Korea (NRF-2019R1A6A1A10073437).

## Appendix A

The integration of Eq. (5) over raindrop mass  $m$  gives:

$$\begin{aligned} \frac{\partial N_r}{\partial t} = & \int_0^{\infty} \int_0^{m'/2} f_r(m', t) f_r(m - m', t) C(m', m - m') dm' dm \\ & - \int_0^{\infty} f_r(m, t) \int_0^{\infty} f_r(m', t) C(m, m') dm' dm \\ & + \frac{1}{2} \int_0^{\infty} \int_0^{\infty} \int_0^{\infty} f_r(m', t) f_r(m'', t) B(m', m'') P(m; m', m'') dm' dm'' dm \\ & - \int_0^{\infty} f_r(m, t) \int_0^{\infty} f_r(m', t) B(m, m') dm' dm. \end{aligned} \quad (\text{A.1})$$

Note that  $C(m, m')$  is a symmetric function of the two raindrop masses. Then, the raindrop mass variables in the first term on the right-hand side of (A.1) are substituted by  $m - m' \rightarrow M$  and  $m' \rightarrow m$ , and those in the second term and fourth term are substituted by  $m \rightarrow M$  and  $m' \rightarrow m$ . For the third term, the integration of  $P(m; m', m'')$  over the whole range of  $m$  gives  $\bar{N}_f(m', m'')$ , and then the raindrop mass variables are substituted by  $m' \rightarrow M$  and  $m'' \rightarrow m$ . Eq. (A.1) is rewritten as

$$\begin{aligned} \frac{\partial N_r}{\partial t} = & \int_0^{\infty} \int_0^M f_r(m, t) f_r(M, t) C(m, M) dm dM \\ & - \int_0^{\infty} \int_0^{\infty} f_r(m, t) f_r(M, t) C(m, M) dm dM \\ & + \frac{1}{2} \int_0^{\infty} \int_0^{\infty} \int_0^{\infty} f_r(m, t) f_r(M, t) B(m, M) \bar{N}_f(m, M) dm dM \\ & - \int_0^{\infty} \int_0^{\infty} f_r(m, t) f_r(M, t) B(m, M) dm dM. \end{aligned} \quad (\text{A.2})$$

Eq. (A.2) is reduced to

$$\begin{aligned} \frac{\partial N_r}{\partial t} = & - \int_0^{\infty} \int_0^M f_r(m, t) f_r(M, t) C(m, M) dm dM \\ & + \frac{1}{2} \int_0^{\infty} \int_0^{\infty} f_r(m, t) f_r(M, t) B(m, M) [\bar{N}_f(m, M) - 2] dm dM, \end{aligned} \quad (\text{A.3})$$

which is rewritten as Eq. (6) by using raindrop radius variables instead of mass variables.

**Table A1**

List of symbols.

Symbol	Description	Value	Unit
$A_j$	Coefficients in Eqs. (12), (13), and (14)	(1, 2, 1)	
$a_0$	Coefficient in Eq. (9)	$7.50 \times 10^{-1}$	
$a_1$	Coefficient in Eq. (9)	$3.54 \times 10^5$	$\text{m}^{-2}$
$a_2$	Coefficient in Eq. (9)	$9.85 \times 10^{-1}$	
$a_3$	Coefficient in Eq. (9)	3.61	$\text{m}^{-a_4}$
$a_4$	Coefficient in Eq. (9)	$2.13 \times 10^{-1}$	
$a_5$	Coefficient in Eq. (9)	$4.30 \times 10^3$	$\text{m}^{-1}$
$B(r, R)$	Breakup kernel between two raindrops with radii $r$ and $R$		$\text{m}^{-3} \text{s}^{-1}$
$B_j$	Coefficients in Eq. (15)	$(-a_2, 1 - 2a_2, 2 - a_2, 1)$	
$b_0$	Coefficient in Eq. (10)	$5.00 \times 10^{19}$	$\text{m}^{-6}$
$b_1$	Coefficient in Eq. (10)	$5.26 \times 10^1$	$\text{m}^{-1}$
$b_2$	Coefficient in Eq. (10)	$2.89 \times 10^3$	$\text{m}^{-1}$
$b_3$	Coefficient in Eq. (10)	$1.50 \times 10^{65}$	$\text{m}^{-18}$
$b_4$	Coefficient in Eq. (10)	$1.16 \times 10^4$	$\text{m}^{-1}$
$b_5$	Coefficient in Eq. (10)	$2.09 \times 10^4$	$\text{m}^{-1}$

(continued on next page)

**Table A1 (continued)**

Symbol	Description	Value	Unit
$C(r, R)$	Coalescence kernel between two raindrops with radii $r$ and $R$		$\text{m}^{-3} \text{s}^{-1}$
$c_{j,i}$	Coefficients in Eq. (12)	in Table 1	
$D$	Particle diameter		$\text{mm}$
$D_{m,r}$	Mass-weighted mean diameter of raindrops		$\text{mm}$
$f_x(R)$	Number concentration of hydrometeor $x$ of radius $R$		$\text{m}^{-4}$
$L_x$	Mass content of hydrometeor $x$		$\text{kg m}^{-3}$
$m, m', m''$	Particle mass		$\text{kg}$
$N_x$	Number concentration of hydrometeor $x$		$\text{m}^{-3}$
$N_{0,x}$	Intercept parameter of gamma size distribution of hydrometeor $x$		$\text{m}^{-4}$
$\bar{N}_f(r, R)$	Average number of fragment drops with any size as a result of the collision between two raindrops with radii $r$ and $R$		
$P(m; m', m'')$	Average number of fragment drops with mass $m$ produced as a result of the collision of two raindrops with masses $m'$ and $m''$		
$q_v$	Water vapor mixing ratio		$\text{g kg}^{-1}$
$R, r$	Particle radius		$\text{m}$
$v_{t,x}$	Terminal velocity of hydrometeor $x$		$\text{m s}^{-1}$
$v_{0,c}$	Coefficient in terminal velocity relation of cloud droplets	1.0973 × 10 <sup>8</sup>	$\text{m}^{-1} \text{s}^{-1}$
$v_{0,r}$	Coefficient in terminal velocity relation of raindrops	9.770	$\text{m s}^{-1}$
$\Gamma$	Complete gamma function		
$\gamma_r$	Coefficient in terminal velocity relation of raindrops	1.097 × 10 <sup>3</sup>	$\text{m}^{-1}$
$\eta_{\text{break}}$	Breakup efficiency		
$\eta_{\text{coal}}$	Coalescence efficiency		
$\eta_{\text{coll}}$	Collision efficiency		
$\theta$	Potential temperature		$\text{K}$
$\lambda_x$	Slope parameter of gamma size distribution of hydrometeor $x$		$\text{m}^{-1}$
$\mu_c$	Shape parameter of gamma size distribution of cloud droplets		
$\mu_r$	Shape parameter of gamma size distribution of raindrops	min[15, nint(10 <sup>9</sup> /N <sub>c</sub> + 2)]	
$\rho$	Air density	1	$\text{kg m}^{-3}$
$\rho_0$	Reference air density	1.185	$\text{kg m}^{-3}$

## References

- Ahmed, T., Jin, H.-G., Baik, J.-J., 2020. A physically based raindrop–cloud droplet accretion parameterization for use in bulk microphysics schemes. *Q. J. R. Meteorol. Soc.* 146, 3368–3383.
- Beard, K.V., 1976. Terminal velocity and shape of cloud and precipitation drops aloft. *J. Atmos. Sci.* 33, 851–864.
- Beard, K.V., Grover, S.N., 1974. Numerical collision efficiencies for small raindrops colliding with micron size particles. *J. Atmos. Sci.* 31, 543–550.
- Beard, K.V., Ochs III, H.T., 1995. Collisions between small precipitation drops. Part II: formulas for coalescence, temporary coalescence, and satellites. *J. Atmos. Sci.* 52, 3977–3996.
- Beheng, K.D., 1994. A parameterization of warm cloud microphysical conversion processes. *Atmos. Res.* 33, 193–206.
- Cohard, J.M., Pinty, J.P., 2000. A comprehensive two-moment warm microphysical bulk scheme. I: description and tests. *Q. J. R. Meteorol. Soc.* 126, 1815–1842.
- Feingold, G., Tzivion, S., Levin, Z., 1988. Evolution of raindrop spectra. Part I: solution to the stochastic collection/breakup equation using the method of moments. *J. Atmos. Sci.* 45, 3387–3399.
- Gaudet, B.J., Schmidt, J.M., 2005. Assessment of hydrometeor collection rates from exact and approximate equations. Part I: a new approximate scheme. *J. Atmos. Sci.* 62, 143–159.
- Hoffmann, F., Noh, Y., Raasch, S., 2017. The route to raindrop formation in a shallow cumulus cloud simulated by a Lagrangian cloud model. *J. Atmos. Sci.* 74, 2125–2142.
- Hu, Z., Srivastava, R.C., 1995. Evolution of raindrop size distribution by coalescence, breakup, and evaporation: Theory and observations. *J. Atmos. Sci.* 52, 1761–1783.
- Jin, H.-G., Baik, J.-J., 2020. A new parameterization of the accretion of cloud water by snow and its evaluation through simulations of mesoscale convective systems. *J. Atmos. Sci.* 77, 2885–2903.
- Kessler, E., 1969. On the distribution and continuity of water substance in atmospheric circulations. In: *Meteor. Monogr.*, 32, Vol. 10. American Meteorological Society, Boston, Mass (88 pp.).
- Khain, A., Pokrovsky, A., Pinsky, M., Seifert, A., Phillips, V., 2004. Simulation of effects of atmospheric aerosols on deep turbulent convective clouds using a spectral microphysics mixed-phase cumulus cloud model. Part I: model description and possible applications. *J. Atmos. Sci.* 61, 2963–2982.
- Khain, A., Rosenfeld, D., Pokrovsky, A., Blahak, U., Ryzhkov, A., 2011. The role of CCN in precipitation and hail in a mid-latitude storm as seen in simulations using a spectral (bin) microphysics model in a 2D dynamic frame. *Atmos. Res.* 99, 129–146.
- Khairoutdinov, M., Kogan, Y., 2000. A new cloud physics parameterization in a large-eddy simulation model of marine stratocumulus. *Mon. Weather Rev.* 128, 229–243.
- Kogan, Y., 2013. A cumulus cloud microphysics parameterization for cloud-resolving models. *J. Atmos. Sci.* 70, 1423–1436.
- Kogan, Y., Ovchinnikov, M., 2020. Formulation of autoconversion and drop spectra shape in shallow cumulus clouds. *J. Atmos. Sci.* 77, 711–722.
- Köhler, H., 1936. The nucleus in and the growth of hygroscopic droplets. *Trans. Faraday Soc.* 32, 1152–1161.
- Kuba, N., Seiki, T., Suzuki, K., Roh, W., Satoh, M., 2020. Evaluation of rain microphysics using a radar simulator and numerical models: comparison of two-moment bulk and spectral bin cloud microphysics schemes. *J. Adv. Model. Earth Syst.* 12, e2019MS001891.
- Lee, H., Baik, J.-J., 2017. A physically based autoconversion parameterization. *J. Atmos. Sci.* 74, 1599–1616.
- Lim, K.-S.S., Hong, S.-Y., 2010. Development of an effective double-moment cloud microphysics scheme with prognostic cloud condensation nuclei (CCN) for weather and climate models. *Mon. Weather Rev.* 138, 1587–1612.
- Low, T.B., List, R., 1982. Collision, coalescence and breakup of raindrops. Part II: Parameterization of fragment size distributions. *J. Atmos. Sci.* 39, 1607–1619.
- McFarquhar, G.M., 2004. A new representation of collision-induced breakup of raindrops and its implications for the shapes of raindrop size distributions. *J. Atmos. Sci.* 61, 777–794.
- Michibata, T., Takemura, T., 2015. Evaluation of autoconversion schemes in a single model framework with satellite observations. *J. Geophys. Res. Atmos.* 120, 9570–9590.
- Milbrandt, J.A., Yau, M.K., 2005. A multimoment bulk microphysics parameterization. Part II: a proposed three-moment closure and scheme description. *J. Atmos. Sci.* 62, 3065–3081.
- Morrison, H., Grabowski, W.W., 2007. Comparison of bulk and bin warm-rain microphysics models using a kinematic framework. *J. Atmos. Sci.* 64, 2839–2861.
- Morrison, H., Grabowski, W.W., 2008. Modeling supersaturation and subgrid-scale mixing with two-moment bulk warm microphysics. *J. Atmos. Sci.* 65, 792–812.
- Morrison, H., Milbrandt, J.A., 2015. Parameterization of cloud microphysics based on the prediction of bulk ice particle properties. Part I: scheme description and idealized tests. *J. Atmos. Sci.* 72, 287–311.
- Morrison, H., Curry, J.A., Khorostyanov, V.I., 2005. A new double-moment microphysics parameterization for application in cloud and climate models. Part I: description. *J. Atmos. Sci.* 62, 1665–1677.
- Morrison, H., van Lier-Walqui, M., Fridlind, A.M., Grabowski, W.W., Harrington, J.Y., Hoose, C., et al., 2020. Confronting the challenge of modeling cloud and precipitation microphysics. *J. Adv. Model. Earth Syst.* 12, e2019MS001689.
- Naumann, A.K., Seifert, A., 2016. Evolution of the shape of the raindrop size distribution in simulated shallow cumulus. *J. Atmos. Sci.* 73, 2279–2297.
- Noh, Y., Oh, D., Hoffmann, F., Raasch, S., 2018. A cloud microphysics parameterization for shallow cumulus clouds based on Lagrangian cloud model simulations. *J. Atmos. Sci.* 75, 4031–4047.
- Nuijens, L., Stevens, B., Siebesma, A.P., 2009. The environment of precipitating shallow cumulus convection. *J. Atmos. Sci.* 66, 1962–1979.
- Paukert, M., Fan, J., Rasch, P.J., Morrison, H., Milbrandt, J.A., Shpund, K., Khain, A., 2019. Three-moment representation of rain in a bulk microphysics model. *J. Adv. Model. Earth Syst.* 11, 257–277.
- Pinsky, M., Khain, A., Shapiro, M., 2001. Collision efficiency of drops in a wide range of Reynolds numbers: effects of pressure on spectrum evolution. *J. Atmos. Sci.* 58, 742–764.

- Prat, O.P., Barros, A.P., 2007. A robust numerical solution of the stochastic collection-breakup equation for warm rain. *J. Appl. Meteorol. Climatol.* 46, 1480–1497.
- Prat, O.P., Barros, A.P., Testik, F.Y., 2012. On the influence of raindrop collision outcomes on equilibrium drop size distributions. *J. Atmos. Sci.* 69, 1534–1546.
- Rauber, R.M., Stevens, B., Ochs III, H.T., Knight, C., Albrecht, B.A., Blyth, A.M., et al., 2007. Rain in shallow cumulus over the ocean: the RICO campaign. *Bull. Am. Meteorol. Soc.* 88, 1912–1928.
- Schrottke, J., Straub, W., Beheng, K.D., Gomaa, H., Weigand, B., 2010. Numerical investigation of collision induced breakup of raindrops. Part I: methodology and dependencies on collision and eccentricity. *J. Atmos. Sci.* 67, 557–575.
- Seifert, A., Beheng, K.D., 2006. A two-moment cloud microphysics parameterization for mixed-phase clouds. Part 1: model description. *Meteorol. Atmos. Phys.* 92, 45–66.
- Seifert, A., Khain, A., Blahak, U., Beheng, K.D., 2005. Possible effects of collisional breakup on mixed-phase deep convection simulated by a spectral (bin) cloud model. *J. Atmos. Sci.* 62, 1917–1931.
- Seifert, A., Blahak, U., Buhr, R., 2014. On the analytic approximation of bulk collision rates of non-spherical hydrometeors. *Geosci. Model Dev.* 7, 463–478.
- Skamarock, W.C., Klemp, J.B., Dudhia, J., Gill, D.O., Barker, D.M., Duda, M.G., et al., 2008. A description of the Advanced Research WRF version 3. In: NCAR Tech. Note NCAR/TN-475+STR (113 pp.).
- Straub, W., Beheng, K.D., Seifert, A., Schrottke, J., Weigand, B., 2010. Numerical investigation of collision-induced breakup of raindrops. Part II: parameterizations of coalescence efficiencies and fragment size distributions. *J. Atmos. Sci.* 67, 576–588.
- Thompson, G., Field, P.R., Rasmussen, R.M., Hall, W.D., 2008. Explicit forecasts of winter precipitation using an improved bulk microphysics scheme. Part II: implementation of a new snow parameterization. *Mon. Weather Rev.* 136, 5095–5115.
- Tripoli, G.J., Cotton, W.R., 1980. A numerical investigation of several factors contributing to the observed variable intensity of deep convection over South Florida. *J. Appl. Meteorol.* 19, 1037–1063.
- vanZanten, M.C., Stevens, B., Nuijens, L., Siebesma, A.P., Ackerman, A.S., Burnett, F., et al., 2011. Controls on precipitation and cloudiness in simulations of trade-wind cumulus as observed during RICO. *J. Adv. Model. Earth Syst.* 3, M06001.
- Verlinde, J., Cotton, W.R., 1993. Fitting microphysical observations of nonsteady convective clouds to a numerical model: an application of the adjoint technique of data assimilation to a kinematic model. *Mon. Weather Rev.* 121, 2776–2793.
- Verlinde, J., Flatau, P.J., Cotton, W.R., 1990. Analytical solutions to the collection growth equation: comparison with approximate methods and applications to cloud microphysics parameterization schemes. *J. Atmos. Sci.* 47, 2871–2880.
- Weisman, M.L., Klemp, J.B., 1982. The dependence of numerically simulated convective storms on vertical wind shear and buoyancy. *Mon. Weather Rev.* 110, 504–520.
- Yamaguchi, T., Feingold, G., 2012. Large-eddy simulation of cloudy boundary layer with the Advanced Research WRF model. *J. Adv. Model. Earth Syst.* 4, M09003.